Energy
Advances

Accepted Manuscript

Energy
Advances

rsc.li/energy-advances

Volume 1
Number 1
January 2022

ISSN 2753-1457

ROYAL SOCIETY
OF CHEMISTRY

This is an Accepted Manuscript, which has been through the Royal Society of Chemistry peer review process and has been accepted for publication.

Accepted Manuscripts are published online shortly after acceptance, before technical editing, formatting and proof reading. Using this free service, authors can make their results available to the community, in citable form, before we publish the edited article. We will replace this Accepted Manuscript with the edited and formatted Advance Article as soon as it is available.

You can find more information about Accepted Manuscripts in the Information for Authors.

Please note that technical editing may introduce minor changes to the text and/or graphics, which may alter content. The journal's standard Terms & Conditions and the Ethical guidelines still apply. In no event shall the Royal Society of Chemistry be held responsible for any errors or omissions in this Accepted Manuscript or any consequences arising from the use of any information it contains.

ROYAL SOCIETY
OF CHEMISTRY

rsc.li/energy-advances

Energy

Advances

ARTICLE

Heterogeneous Aging in a Multi-cell Lithium-ion Battery System Driven by Manufacturing-induced Variability in Electrode Microstructure: A Physics-Based Simulation Study

Parisa Akhtari Zavareh[a], Aditya Naveen Matam [b] and Krishna Shah[a,*]

[a] Department of Mechanical Engineering, The University of Alabama, Tuscasloosa

[b] Department of Electrical and Computer Engineering, The University of Texas at Austin

[*] Corresponding Author

Heterogeneous aging of lithium-ion battery cells within a battery pack is a major challenge that limits the pack's overall performance, safety, and life. Variations in cell degradation rates lead to nonuniform charge/discharge behavior among cells in a pack, accelerated aging in some cells turning them into "weak links", and reducing energy throughput at the pack level. While previous studies have investigated uneven aging driven by differences in capacity or resistance, limited attention has been given to the root causes of these variations, particularly those arising from manufacturing-induced differences in the electrode microstructure. This study addresses this gap by investigating the effects of variations in active material particle size, a key design parameter of a porous electrode, on the aging behavior of battery cells connected in series and parallel. Using an electrochemical battery model, the aging behavior of individual cells and the pack as a whole is investigated for three electrical configurations (i.e., 1S4P, 4S1P, and 2S2P) at select C-rates and voltage windows. Results indicate that cells with smaller particle radii degrade faster despite having a thinner SEI layer at the end of life, and a minor variation of even 1 µm in the active material particle size can lead to significant uneven capacity fade across cells and accelerated aging of the pack, particularly at low C-rates. These findings highlight the critical impact that variability in the microstructure has on pack-level aging and provide insights into effective cell and pack manufacturing.

Introduction:

Since their commercialization in the early 1990s, Lithium-ion batteries have gained popularity because of their excellent characteristics, including high-energy density, power density, and long cycle life.[1-3] Initially utilized in personal electronics devices, their applications have expanded into transportation and industrial sectors, particularly for electric vehicles (EVs) and energy storage .[3] A variety of cell chemistries have been proposed as promising candidates for these applications, each with distinct performance characteristics and limitations.[3-4] Although Li-ion batteries have various advantages and are utilized in a wide range of applications, there remain challenges related to their material degradation, loss of performance due to aging, and safety issues.[1, 2, 5] Aging and degradation are the key challenges among these, as they directly impact the battery's lifespan, charge/discharge performance, and safety.[5] As batteries age, various degradation mechanisms will take place such as solid electrolyte interphase (SEI) layer growth, Lithium plating, dendrite growth, and electrode material breakdown, all leading to capacity fade, power loss, and reduction in roundtrip efficiency.[6] Degradation in Li-ion batteries can lead to significant safety concerns, including fires, explosions, and system-level failures.[2, 5, 6] For example, the National Highway Traffic Safety Administration (NHTSA) announced the recall issued by Tesla Motors for approximately 53,000 of their Model S vehicles due to the risk of battery module failure.[34] The primary cause of battery module failure was dendrite formation in the Li-ion battery cells, which poses a safety risk due to the possibility of an internal short circuit .[34] Beyond safety concerns, battery degradation also poses economic and environmental challenges, as it necessitates more frequent replacements, increasing production and recycling burdens.[1, 3] The need for more frequent replacement of battery packs due to capacity fade and performance degradation leads to an increase in the overall cost of ownership for consumers and the manufacturer.[35] The exponential growth in the production of Li-ion batteries to meet the growing demand necessitates effective recycling strategies to minimize raw material mining and prevent the negative impact on the environment due to improper disposal of batteries in the landfill.[5]

A large body of work is reported in the literature on Li-ion battery material degradation and aging .[33, 36-45] Experimental studies on Li-ion battery degradation have identified several mechanisms impacting battery performance.[12-15, 22-25] Metal oxide dissolution leads to capacity fade and increased cell polarization, as observed in past studies done through electrochemical testing.[12] State of charge (SOC) and temperature affect calendar aging, while SOC swing, current, and temperature affect cycle aging.[13] Investigation of NMC/graphite battery cells under various operating conditions using impedance spectroscopy and electrochemical analysis indicates an increase in solution and charge transfer resistance during cycling, with a high C-rate significantly promoting an increase in the resistance arising from diffusion.[22] Electrochemical impedance spectroscopy and cycling tests were conducted on commercial NMC Li-ion cells under a standardized real-world driving profile at 45°C and 10°C.[23] This study shows that there is an increase in capacity fade and internal resistance because of Lithium loss and SEI formation.[23]

Impedance studies of NMC/graphite cells at 0°C, 22°C, and 45°C under realistic automotive operating conditions with fast charging at 2C show a decrease in charge transfer resistance in initial aging stages at low temperatures that might be linked to increased double-layer capacitance.[24] Also, at low temperatures (e.g., at ±0°C), an increase in the peak power is reported, indicating the complex role of temperature in aging.[24] Elevated temperatures and upper cut-off voltages lead to increased rate of SEI growth and cell impedance, resulting in accelerated aging, as confirmed by electrochemical methods, X-ray diffraction (XRD), and Prompt-Gamma-Activation-Analysis (PGAA).[25] In silicon-doped graphite and NCA cathode cells, post-mortem analysis and electrochemical testing indicate that depth-of-discharge significantly affects cycle life.[14] Lower charging rates can accelerate aging under certain conditions, such as when the battery is charged to a high SOC during cycling. This is exacerbated at elevated temperatures (e.g., 60°C) and high depth of discharge.[14] Trippetta et al.[15] used a combination of cross-sectional scanning electron microscopy (SEM), nuclear magnetic resonance (NMR), and electrochemical measurements to study heterogeneous aging in high-energy Li-ion batteries with silicon-graphite composite negative electrode, revealing uneven degradation across different cell areas.[15]

Numerical studies have complemented experimental work by providing deeper insight into the degradation mechanisms of Li-ion batteries.[15-17] To better understand aging behavior of active materials during the aging processes, physics-based models have been developed to interpret quasi-OCV data.[15] Sordi et al.[16] developed a physics-based Pseudo-2D (P2D) model to study the effect of variation in model parameters, such as Lithium inventory and reaction rates, on the deterioration of Li-ion batteries under different operating conditions, including temperature fluctuations. Zhang et al.[17] created a 3D simulation model that accurately captures the electrochemical, thermal, and mechanical interactions in cells, simulating spatially varying properties such as SOC and current density. Another study develops a semi-empirical model to study SEI growth during the battery formation and cycling, capturing the irreversible cell expansion, SEI growth, and multi-species reactions.[49] The study highlights how SEI growth consumes cyclable Lithium, increases impedance and irreversible expansion which reduces battery capacity.[49] A porous electrode pseudo two-dimensional (P2D) was reformulated to include SEI growth as a side reaction to study battery degradation under eight driving cycles (including regenerative break) and six charging protocols.[48] Lawder et al.[48] found that regenerative braking can increase the usable energy in some cases, while it can also accelerate capacity fade in others.[48] Additionally, they found a high C-rate and deeper depth of discharge causing increased SEI growth and capacity fade.[48]

A Lithium plating-induced aging model was proposed by Yang et al.[47] to predict the Li-plating degradation mechanism in the Li-ion battery. This study shows that the formation and growth of the SEI layer on the anode surface leads to a decrease in the anode porosity.[47] This leads to an increase in the electrolyte potential gradients, which makes it easier for the metallic Lithium to start plating on the anode particle surface.[47] Another study developed a 2D physics-based model to investigate how design parameters, such as anode thickness, electrolyte conductivity, and tab placement, influence the Lithium plating formation risk in the pouch cell by incorporating the actual winding structure of the Li-ion cell.[46] The study reveals that the inner layers of the anode are more prone to the Li-plating due to overpotential distribution. Moreover, the higher conductivity of electrolyte and Li-ion diffusion in the cathode enhances the risk of Lithium plating, while higher anode diffusivity reduces the Li-plating risk.[46]

The battery systems in many applications, especially EVs, are composed of multiple modules connected in series, forming a battery pack.[6, 9] These modules consist of multiple Li-ion cells connected in series-parallel to fulfill the specific energy and power requirements of the battery-powered system of interest.[9] This makes studying the aging of battery cells in battery packs of significant relevance. Specifically, uneven aging of battery cells in a battery pack poses a key challenge. The uneven aging of battery cells in a pack has implications on the performance, lifespan, and safety of the battery pack. As the large number of cells in a battery pack deteriorate at different rates, the resulting uneven aging can lead to imbalances in performance and charge/discharge capacity, which in turn affect the overall energy efficiency and lifespan of the battery pack.[10, 11] To maximize the performance and lifespan of the battery packs, it is crucial to fully understand and address the challenges that arise from uneven aging of the individual cells and ensure that the aging effects are evenly distributed among the cells within a pack.[11] Despite extensive research on individual cell degradation, there remains a need for further exploration of degradation patterns in battery packs, where uneven cell degradation can worsen overall battery pack performance.[10]

The uneven aging of Li-ion cells within the battery packs is attributed to cell-specific variations, system-level factors, and temperature gradients.[9,10] Cell-specific variations include differences in impedance and capacity within a large batch of cells caused by manufacturing inconsistencies and impurities in raw materials.[9, 10] System-level factors include variations in contact resistance between cells, battery pack design, and cooling system.[9, 26, 28] The imbalance in the current distribution across cells in a pack, which can also lead to overheating in some of the cells, is due to both system-level factors and cell-specific variations.[9-10, 18-20, 26] Past studies have indicated that capacity variations among cells due to the variability in manufacturing result in imbalance in the current distribution within the battery pack.[19, 25-30] Wu.et al.[27] used two cells with different initial capacities in parallel connection and observed that the one with higher capacity carried a larger amount of current during constant current (CC) discharge. Similar findings were reported by J.Brand et al.[28], who investigated two cells with the same internal resistance, but different capacities connected in parallel. They found the cell with smaller capacity undergoing faster changes in SOC, during both charging and discharging, compared to the one with higher capacity, resulting in differences in OCV.[28] The magnitude of the current flowing through individual cells within a pack is also affected by differences in the internal resistance. Bruen et al.[29] studied four cells with different internal resistances connected in parallel configurations and observed that the cells with lower resistance experienced higher currents. This uneven current distribution increases the risk of overloading cells with lower internal resistances, leading them to operate under higher currents and faster degradation compared to the ones with higher internal resistances. Another experimental study conducted on new Panasonic 18650 cells and a retired battery pack from a Mercedes-Benz Vito e-Cell revealed that the capacity and impedance variations among the cells due to manufacturing differences and operating conditions lead to uneven load distribution and accelerated aging.[9] This study also revealed that aged packs exhibited significantly higher capacity and internal resistance variations across cells, which worsened with further cycling by as much as 100% with respect to the variation prior to cycling. The results from this study show that parallel-connected cells do not converge in SOH but instead become more imbalanced over time.[9] Moreover, the temperature gradients within the battery pack have been found to lead to uneven current distributions.[9, 20, 26, 30, 31] A study applying forced temperature gradients to series-connected cells found that colder cells exhibited accelerated aging, which was linked to Lithium plating.[20] This temperature-induced uneven degradation was the primary cause of voltage drift within the module.[20] Another study cycled three parallel-connected LFP cells with different insulation and observed that the cell with higher temperatures, due to the kind of insulation applied, experienced 25% higher currents compared to the one with the lower temperature. This uneven current distribution difference caused accelerated aging of the cell operating at higher temperatures and significant uneven aging at the system level.[33] In addition to capacity and internal resistance, SOC variations among the cells can both result in and contribute to uneven current distribution and uneven aging at the pack level.[31-33] Shi et al. observed an SOC difference of about 7% at the end of charging between two parallel-connected cells, which led to current through one of the cells reach 0.8C, that is 60% higher than the expected value.[32] This study revealed that the imbalanced current distribution, due to SOC variation, causes one cell to experience higher stress, degrade faster, and lead to uneven aging of the parallel-connected cells.[32]

Previous studies have extensively examined degradation phenomena at the single-cell level and, more recently, uneven aging across battery packs caused by factors such as cell-to-cell manufacturing variations, system-level interactions, and temperature gradients. However, existing research on pack-level uneven aging due to manufacturing variability has largely emphasized differences in cell capacity and internal resistance. A critical knowledge gap remains in understanding how variations in intrinsic material properties and design parameters—such as the particle radius of active materials, electrode porosity, and thickness of the electrodes—affect the onset and progression of uneven aging within a pack. Because specific manufacturing processes directly influence these physical and structural properties, evaluating their effects can help identify which manufacturing steps most strongly contribute to variability-induced degradation.

The present study addresses this gap through physics-based simulations that examine how variations in material and design parameters influence uneven aging across multiple pack configurations. Among these parameters, particle radius variation is chosen as a representative manifestation of manufacturing inconsistency for several key reasons. First, particle size directly determines the electroactive surface area available for interfacial reactions, making it central to the modeling of SEI formation and growth, the primary degradation mechanism considered in this work. Second, particle radius controls the diffusion length within active material particles, affecting the local lithium concentration and surface chemical potential, which in turn influence SEI reaction kinetics. Third, particle size distribution is highly sensitive to upstream manufacturing steps such as milling, slurry mixing, and calendaring, and thus represents a realistic and practically significant source of variability in commercial cell production. In contrast, large variations in porosity or electrode thickness would proportionally alter the nominal capacity of individual cells, and cells exhibiting such deviations are typically excluded from pack assembly. Moreover, even small absolute differences in particle size correspond to substantial relative variations at the microscale, amplifying their influence on interfacial kinetics and long-term degradation behavior. Finally, the role of particle-size heterogeneity on pack-level aging dynamics remains largely unexplored, providing an opportunity to establish a clear cause–effect relationship between microstructural variability and emergent uneven aging behavior.

Accordingly, this study investigates particle-size-induced uneven aging across a wide range of operating conditions (C-rate, charge/discharge voltage window) and electrical configurations of Li-ion battery packs. Although the work focuses primarily on SEI formation and growth, the

modeling framework is extendable to include other degradation mechanisms, offering a systematic foundation for future studies on additional sources of manufacturing variability.

Methodology:

Mathematical Framework:

In this section, we detail the mathematical models that comprise a battery pack. The framework consists of the Single-Particle model (SPM) for each electrode and an electrical model for the coupling of cells in series, parallel configurations. The electrochemical formulation also includes the growth of Solid-Electrolyte Interface (SEI) on the anode surface – which is responsible for capacity fade.

Single Particle Model:

Lithium intercalation in the LCO cathode and Graphite anode is governed by SPM. Both electrodes are represented as lumped spheres that are discretized radially. Interaction with the bulk electrolyte and separator are not considered for simplicity but are the subject of future study. Ubiquitous for a relatively low computational footprint (in comparison to P2D and higher-order models), SPM is favorable for the simulation of battery packs due to the large number of Differential Algebraic Equations (DAEs) that need to be solved. Further, SPM is suitable for performing a large number of Monte-Carlo runs necessary to obtain statistically relevant results.

Cathode Equations:

Fick's Law, given in Eq. (1) is used to model the physical processes of the cell cathode, with a surface boundary condition that accounts for applied current density.

$$\frac{\partial c_p}{\partial t} = -D_p \frac{1}{r^2} \frac{\partial}{\partial r}\left(-r^2 \frac{\partial c_p}{\partial r}\right)$$

$$\begin{cases} \left.\frac{\partial c_p}{\partial r}\right|_{r=0} = 0 \\ \left.\frac{\partial c_p}{\partial r}\right|_{r=R} = -\frac{j_p}{FD} \end{cases} \tag{1}$$

Assuming equal transfer coefficients ($\alpha_c = \alpha_a = 0.5$), the difference of exponential terms in the Butler-Volmer equation, a well-known equation relating reaction current with overpotential, can be rewritten as a hyperbolic sine function in Eq. (3). Eq. (4) details the equation for exchange current density.[50]

$$j_p = j_{0,p} * 2\sinh\left(\frac{F}{2RT}\left(\phi_p - Eq_p\right)\right)$$

$$j_p \equiv \frac{i_{cell}}{a_p L_p F} \tag{2}$$

$$j_{0,n} = k_p \left(c_{surf,p}\right)^{0.5} \left(c_{max,p} - c_{surf,p}\right)^{0.5} \tag{3}$$

Anode Equations:

Fick's Law is used to model the physical processes of the cell anode. The governing equations are largely like those of the cathode. Additional equations are coupled with SPM to model the growth of the SEI layer on the anode surface during charge.

$$\frac{\partial c_n}{\partial t} = -D_n \frac{1}{r^2} \frac{\partial}{\partial r}\left(-r^2 \frac{\partial c_n}{\partial r}\right) \tag{4}$$

$$\begin{cases} \left.\dfrac{\partial c_n}{\partial r}\right|_{r=0} = 0 \\ \left.\dfrac{\partial c_n}{\partial r}\right|_{r=R} = -\dfrac{j_n}{FD} \end{cases}$$

The Butler-Volmer equation, Eq. (5), governs the electrochemical potential of the anode, modified to include ionic resistance introduced by SEI growth:[50]

$$i_{n,int} = j_{0,n}\left[exp\left(\frac{\alpha_c F}{RT}\left(\phi_n - Eq_n - \frac{\delta}{\kappa_{sei}}j_n\right)\right) -- exp\left(\frac{-\alpha_a F}{RT}\left(\phi_n - Eq_n - \frac{\delta}{\kappa_{sei}}j_n\right)\right)\right] \tag{5}$$

Assuming equal transfer coefficents ($\alpha_c = \alpha_a = 0.5$), the difference of exponential terms is rewritten as a hyperbolic sine function in Eq. (6). Eq. (7) details the equation for anode exchange current density:[50]

$$i_{n,int} = j_{0,n} * 2sinh\left(\frac{F}{2RT}\left(\phi_n - Eq_n - \frac{\delta}{\kappa_{sei}}j_n\right)\right) \tag{6}$$

$$j_n \equiv -\frac{i_{cell}}{a_n L_n F}$$

$$j_{0,n} = k_n\left(c_{surf,n}\right)^{0.5}\left(c_{max,n} - c_{surf,n}\right)^{0.5} \tag{7}$$

This study investigates capacity fade over several charge/discharge cycles. Formation of the SEI layer on the anode during charging is responsible for significant degradation in Lithium-ion batteries; the physics and parameters governing SEI-driven aging are taken from literature.[50]

The growth of the SEI layer is driven by a deviant side-current, i_s, that is a small fraction of the total applied current to the anode (Eq (8)). The relationship between the side-current and its corresponding voltage drop is given by the Tafel-like kinetics expression in Eq. (9).

$$\frac{d\delta}{dt} = -\frac{i_s}{2F}\frac{M_{sei}}{\rho_{sei}} \tag{8}$$

$$j_n = i_{n,int} + i_s$$

$$i_s = -Fk_{f,s}c_{EC}\exp\left(-\frac{\beta_s F}{RT}\left(\phi_n - \frac{\delta}{\kappa_{sei}}j_n\right)\right) \tag{9}$$

Electrical Coupling of Cells -- Pack Formulation:

For most applications, battery packs consist of cells that are interconnected in series and in parallel. This is done to increase operating voltage and charge capacity, respectively. Ubiquitous circuit laws are applied to establish the coupling between cell voltages and cell currents that comprise a pack.
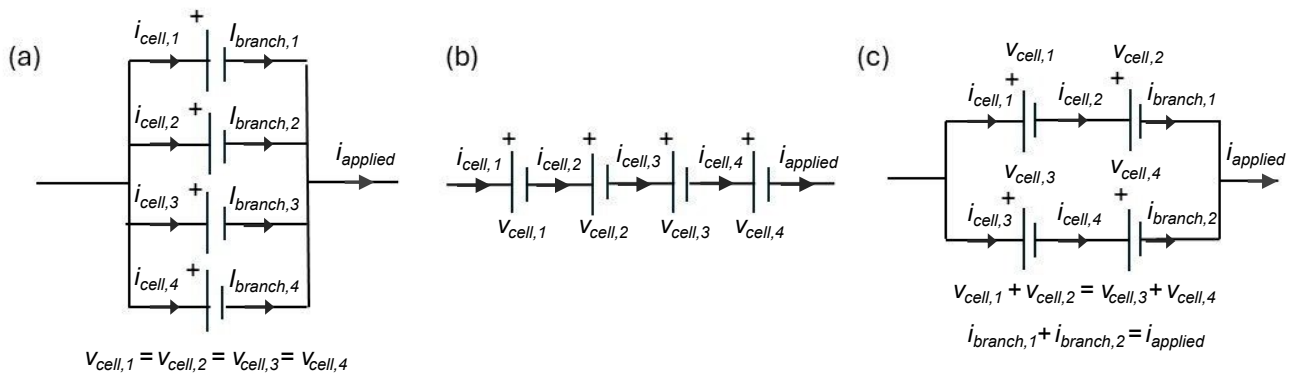
Fig. 1: Schematic representation of a battery pack with an electrical configuration of (a): 1S4P, (b): 4S1p and (c): 2S2P.

By Kirchhoff's Current Law in Eq. (10), the local current on each parallel branch must sum to the total applied current to the pack:

$$i_{applied} = \sum_{i=1}^{M} i_{branch,(i)} \tag{10}$$

By continuity of current in Eq. (11), the applied current density to each cell in series (i.e. along a branch) must be identical. Note the i_{cell} term is referenced in the anode and cathode equations in their respective definitions of electrode current density.

$$i_{cell,(i,1)} = i_{cell,(i,2)} = \cdots = i_{cell,(i,N)} = i_{branch,(i)} \quad i \in \{0,1,\dots,M\} \tag{11}$$

By Kirchhoff's Voltage Law in Eq. (12), the voltage drops across each parallel branch must be identical.

$$\sum_{j=1}^{N} V_{cell,(1,j)} = \sum_{j=1}^{N} V_{cell,(2,j)} = \cdots = \sum_{j=1}^{N} V_{cell,(M,j)} \tag{12}$$

The formulations in Eq. 10 and Eq. 12 are consolidated to be passed to a DAE solver. Each i_{branch} state variable must have a corresponding equation to establish a well-determined system; The final vector of algebraic equations is as follows:

$$0 = i_{applied} - \sum_{i=1}^{M} i_{\text{branch},(i)}$$

$$0 = \sum_{j=1}^{N} V_{\text{cell},(2,j)} - \sum_{j=1}^{N} V_{\text{cell},(1,j)}$$

$$0 = \sum_{j=1}^{N} V_{\text{cell},(3,j)} - \sum_{j=1}^{N} V_{\text{cell},(2,j)}$$

$$\dots$$

$$0 = \sum_{j=1}^{N} V_{\text{cell},(M,j)} - \sum_{j=1}^{N} V_{\text{cell},(M-1,j)}$$

$$\begin{cases} 0 = i_{applied} - \sum_{i=1}^{M} i_{\text{branch},(i)} \\ 0 = \sum_{j=1}^{N} V_{\text{cell},(i,j)} - \sum_{j=1}^{N} V_{\text{cell},(i-1,j)}, \qquad i \in [2,M] \end{cases} \tag{13}$$

$M:=$total number of parallel branches

$N:=$total number of series elements

$(x,y):=$indices for cells in a pack grid;

x-th parallel branch, y-th cell in the branch

$V_{\text{cell}}:=\phi_p - \phi_n$

Simulation Methodology:

In the current study, two approaches were considered to assign variations in the electrode particle radius across the cells within the battery pack to investigate how manufacturing variations influence the uneven aging of the battery pack. In the first approach, the particle radius of each cell within the battery pack was picked by implementing the random sampling from a normal (Gaussian) distribution. A nominal particle radius of both positive and negative electrodes is 2 μm and three different target variabilities of 10%, 20%, and 30% were set as a percentage of variation. For each cell, a random value was assigned from the standard normal distribution using MATLAB's "randn" function, scaled by the introduced variation, and added to the nominal value of particle radius:

$$R_{n,i} = R_{n,0} + \sigma + \delta_i \tag{14}$$

This approach produces a symmetric spread of particle radius centered around the nominal value, permitting the simulation to explore general variability trends.

The second approach aimed to select the extreme particle radius values for each variation to investigate the worst-case scenario of uneven aging of the battery pack. In the second approach, the same nominal particle radius and standard deviation were used. However, instead of sampling freely, the z-scores from controlled extreme ranges were assigned. Here, some cells are assigned a larger than nominal particle radius by choosing z-scores uniformly from the [2, 3] interval, corresponding to values 2 to 3 standard deviations above the mean. Meanwhile, values smaller than the nominal particle radius were assigned to the rest of the cells, and these values were selected from the z-score interval of [-3, -2], which included values 2 to 3 standard deviations below the mean. This combination of high and low extremes creates a battery pack with intentionally maximized variability, which is designed to exacerbate cell-to-cell variations and their effects on the aging of the battery pack. Since each battery pack comprises four cells, there are multiple possible combinations of large and small particle radii, including configurations with two large and two small cells, one large and three small, or one small and three large. The combination that produces the greatest degree of uneven aging among the cells was chosen. This extreme combination varies based on the electrical configuration (1S4P, 4S1P, or 2S2P), as the interaction between cell connection type and particle size distribution affects the aging process within the pack. This study discusses in detail the results and implications of the second approach, which represents the worst-case scenario of cell-to-cell variation to highlight how extreme particle size differences can intensify uneven aging across cells and at the pack level.

As explained in the preceding paragraphs, the particle radius variations in this study were randomly assigned for each simulation; as a result, a single run is insufficient to guarantee statistically reliable results. To ensure that the outcomes reflected robust trends rather than random fluctuations, simulations were repeated multiple times. After each set of runs, the standard deviation and standard error (SE) of the capacity across cells were calculated based on the following equations:

$$\sqrt{\frac{1}{n+1} + \sum_{i=1}^{n}(x_i - x)^2} \tag{15}$$

Where x_i is the capacity of the ith cell, x is the mean capacity, and n is the number of independent runs.

$$SE = \frac{\sigma}{\sqrt{n}} \tag{15}$$

Where σ is a standard deviation of the cells' capacities across the simulation runs, n in the denominator of the fraction represents the number of independent runs. Simulations continued running until the computed SEM dropped below a preset threshold of 5%, ensuring statistical convergence. This approach allowed for confident reporting of average capacities and aging trends that were not biased by stochastic sampling. By applying this convergence criterion, there is a high likelihood that the number of runs used for each case study (1S4P, 4S1P, 2S2P) was sufficient to capture the effects of manufacturing variation on battery pack aging with high statistical reliability.

To validate the SEI model implemented in this study, we compared its predictions with results from the multimodal physics-based aging model presented by Safari and Delacourt.[50] The comparison confirms consistency in SEI growth behavior, and supporting figures are provided in the supplementary material (Fig. S12).

Results and Discussion:

Using the modeling framework and simulation methodology discussed in the Methodology section, we investigated the effect of variation in electrode active material particle size across a 4-cell Lithium-ion battery pack on the overall aging behavior of the pack as well as the individual cells in the pack. We considered three different electrical configurations, namely 1S4P, 4S1P, and 2S2P, to understand how the type of interconnection among cells (i.e., series, parallel, and a combination of the two) may influence the complex interactions between cells. The results, in turn, would dictate the aging behavior and trajectory of the individual cells and the pack. The extent of how manufacturing
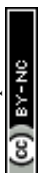
variation in the particle radius affects the aging trajectory of the pack and the standard deviation in the cell charge capacity across cells in the pack over the pack lifetime were studied for all configurations. Three manufacturing variation scenarios with three different standard deviations in the particle radius corresponding to 10%, 20%, and 30% of the base particle radius were considered.

As 1S4P entails all cells operating at the same terminal voltage but drawing different currents, this configuration was studied at two different C-rates to determine how the magnitude of total current applied could influence the current distribution across cells, and as a result, the aging characteristics of the cells and the pack. Based on similar reasoning, in the case of 4S1P, two different voltage windows were analyzed. Two C-rates and voltage windows in the case of 2S2P configuration were considered, as this configuration involves both voltage variation and current variation across cells.

All parallel electrical configuration - 1S4P:

The first case study involved a battery pack with a 1S4P electrical configuration cycled at two C-rates, 0.1C and 1C, using the simulation methodology detailed previously. This case study was undertaken to understand how the variation in particle radii across cells operating at the same terminal voltage influences the current individual cells draw/deliver, and how that ultimately affects their aging behavior individually and collectively as a pack.

As shown in Table 1, at the pack level, increasing the standard deviation in the particle radius across cells significantly accelerated capacity fades. At 0.1C, the pack reached 80% of its initial capacity, referred to as end of life (EOL) in the present study, after approximately 2991, 1866, and 1119 cycles for the three standard deviations equaling 10%, 20%, and 30% of base particle radius, respectively. At 1C, the corresponding lifespans were found to be 4986, 3190, and 2601 cycles, respectively, demonstrating a similar effect of increasing standard deviation in the particle radius across cells on the pack aging rate, albeit with overall higher cycle counts for reaching EOL compared to 0.1C. This general trend indicates that although intrinsic manufacturing variability introduces uneven aging potential, the external operating regime, particularly the C-rate in the case of parallel connected cells, plays an important role in determining system-level outcomes.

Table 1. Cycle life of battery packs with 1S4P, 4S1P, and 2S2P configurations under different particle radius variation levels, C-rates, and voltage windows. End-of-life (EOL) is defined as when pack capacity reaches 80% of its initial value.

Pack Electrical Configuration	Particle Radius Variation	2.75-4.2V		3.25-4V	
		0.1C	1C	0.1C	1C
		Cycle Life			
1S4P	10%	2991	4986	NA*	
	20%	1866	3190		
	30%	1119	2601		
4S1P	10%	2847	NA*	3918	NA*
	20%	2667		3510	
	30%	1319		1401	
2S2P	10%	2036	3079	2307	4007
	20%	1764	2919	1956	3592
	30%	815	2021	832	1855

Fig. 2 shows a decline in the charge capacity of all four cells with cycling at two different C-rates for all three particle radius variations. For the 30% variation case at 0.1C, Cell 4, with the smallest particle radius of 0.29 μm, exhibited a dramatic capacity loss of approximately 40% at EOL for the battery pack, while Cells 1 and 3, with the largest particle radii of 3.49 μm and 3.77 μm, respectively, experienced only 9% capacity decay, approximately. For the 20% variation case, the cells with a smaller particle radius cell capacity degraded by around 24–26%, whereas the cells with a larger particle radius degraded only around 15%. Even at a 10% variation case, slight capacity differences emerged, with small-particle cells showing a marginally higher fade. These patterns arose due to SEI growth, a surface-area-driven mechanism, disproportionately affecting the cells with higher specific surface area (i.e., cells with small active material particles), accelerating Lithium consumption, leading to a faster capacity fade. According to Fig. S3, cells with larger particle radii, such as Cell 1 for the 30% variation case,

consistently develop thicker SEI layers because the SEI forms over a smaller surface area. However, this does not imply greater total SEI growth; in fact, smaller-particle cells experience more SEI growth overall due to their significantly larger surface area.

Importantly, when the capacity fade is normalized by the number of cycles, the calculated overall aging rates highlighted the severity of the capacity fade in small-particle cells compared to large-particle cells. Under a 30% variation at 0.1C, Cell 4 degraded at an average rate of around 0.036% per cycle, nearly four times faster than large-particle Cells 1 and 3, which degraded at around 0.008% per cycle. At 1C, the aging rates are markedly lower and more uniform across all cells, ranging between 0.006% and 0.010% per cycle, and the capacity of the individual cells appears to converge and their degradation rates are observed to become more even with cycling. This convergence indicated that the high kinetic demands of higher current rates during the cycling suppressed the manifestation of intrinsic manufacturing differences in terms of SEI based capacity loss, leading the cells to age more evenly over time.
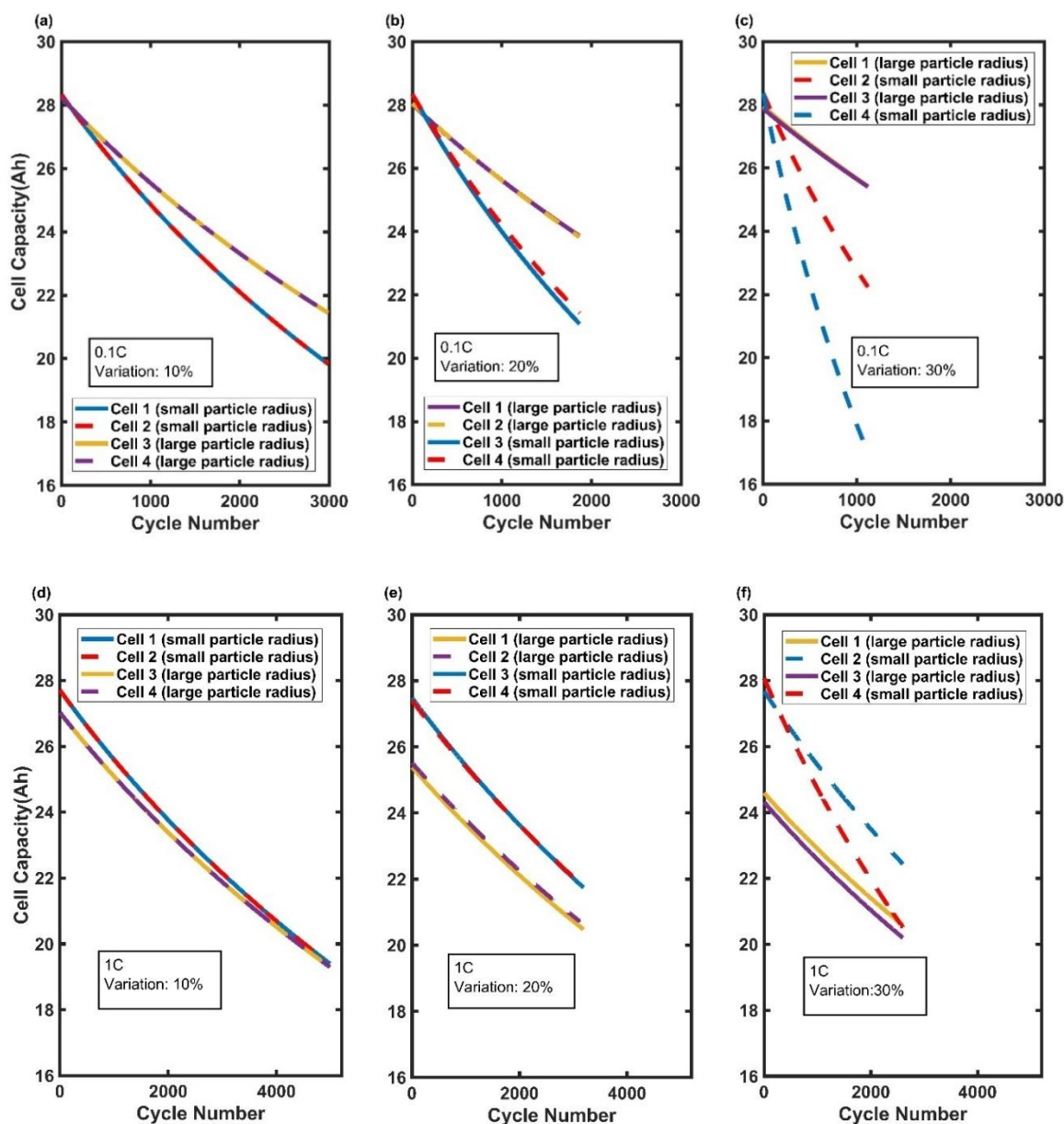

Fig. 2: Cell capacity vs. cycle number for four cells in a battery pack with 1S4P electrical configuration at two different C-rates of 0.1C and 1C under a voltage window of 2.75-4.2 V. Panels (a-c) display capacity fade at 0.1C, and panels (d-f) display capacity fade at 1C.

Fig. 3 indicates the current deviation by plotting scaled current, which is the ratio of actual cell current to the ideal cell current in the absence of cell-to-cell variations. This figure provides detailed information on how current distribution evolves under different levels of variation and current rate. Under 0.1C, particularly at a higher level of variation (i.e., 30%), the system shows significant non-uniform current distribution.

For instance, at 30% particle radii variation and EOL, Cell 1 with a larger particle radius of 3.49 µm exhibited a scaled discharge current as high as 1.6, indicating it provided around 60% more current than its nominal ideal share at times. Cell 4, the one with the smallest particle radius of 0.29 µm, exhibited a scaled current as low as 0.6, which means a contribution of about 60% of the nominal ideal current at times. The same pattern is observed during charging as well, where the cells with a large particle radius reached scaled current as high as 1.4-1.6 at EOL, while the current share of cells with a small particle radius dropped to 0.6-0.8.
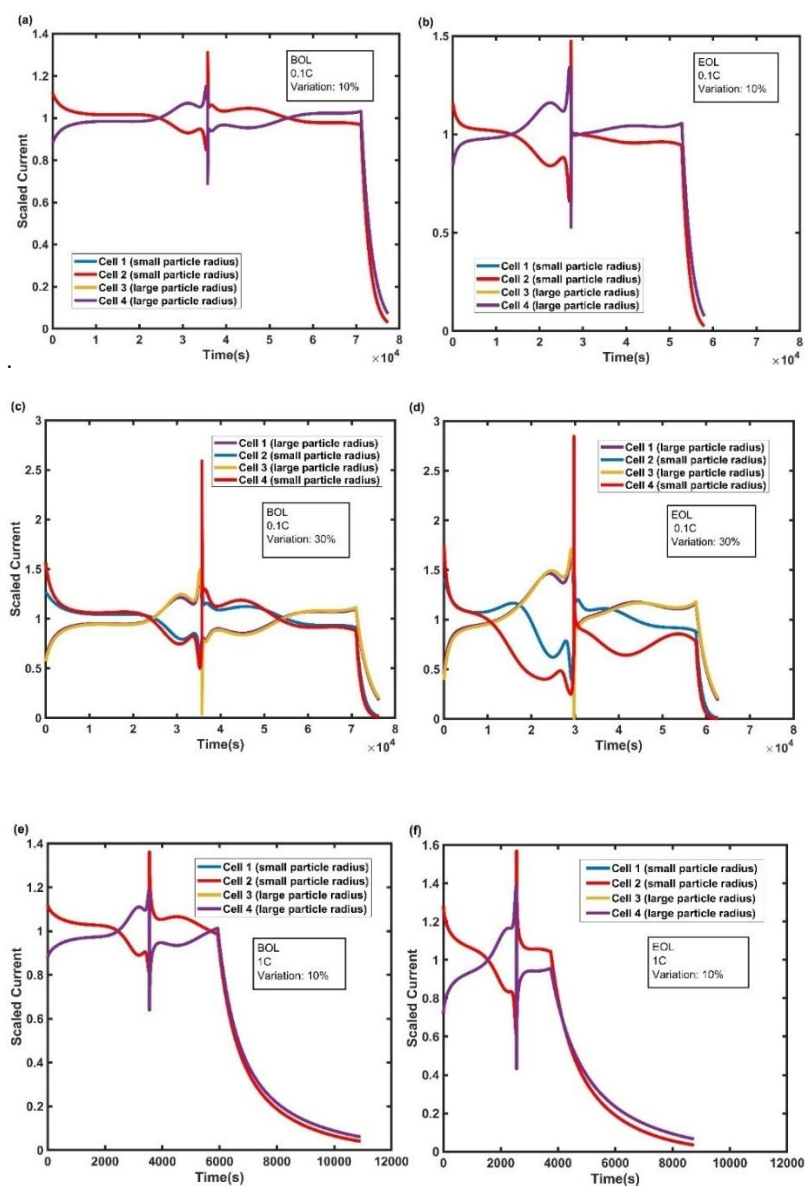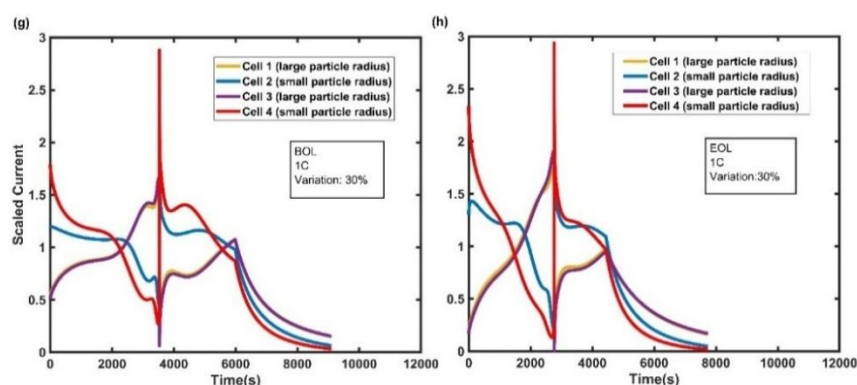
Fig. 3: Scaled current evolution of individual cells at the beginning of life (BOL) and end of life (EOL) for two levels of particle radius variation (i.e., 10% and 30%) under a voltage window of 2.75–4.2 V. Panels (a–d) show the scaled current of the four cells at 0.1C, and panels (e–h) correspond to 1C.

The evolution of anode potential over time, as shown in Fig. S1 and Fig. S2, provided additional insight into the aging behavior observed at the cell level, particularly during the charging phase, as that was when SEI formation occurred. At 0.1C, cells with smaller particle radii exhibit a slight upward shift in anode potential by the end of life (EOL), indicating a higher interfacial resistance due to enhanced SEI growth. However, cells with larger particle radii maintain lower anode potential throughout cycling, which aligns with their lower degradation rates and lesser rate of SEI formation relative to smaller-particle cells. At 1C, the anode potential of cells with larger particle radii dropped more significantly during charging, even becoming negative relative to the Li/Li$^+$ reference indicating a high probability of metallic lithium deposition. This significant downward shift is caused by higher interfacial resistance caused by thicker SEI layers, which impede lithium-ion transport and increase overpotential. It is vital to mention that while the SPM framework can predict anode potential becoming negative, an indicator of high probability of lithium plating, this degradation mechanism cannot be modeled effectively using the SPM framework due to the absence of electrolyte phase in the model. Consequently, although the model captures the SEI-driven resistance growth and capacity loss, it may underestimate the severity of degradation under high C-rate conditions as it neglects additional kinetic limitations and side reactions such as Lithium plating.

Fig. 4 indicates the capacity spread generated from multiple simulation runs to provide a statistically meaningful assessment of how random particle radii variation affects the cells' capacity and the overall battery pack degradation. To ensure this, the simulations were repeated until the standard error of the mean (SEM) across cells' capacities dropped below a threshold of 5%. The plots in the first row, Fig. 4(a, b), show the evolution of the standard deviation (SD) of capacity across cells over the cycle life. The solid line shows the SD averaged over all random draws, while the shaded region shows the statistical spread of the outcomes with greater than 5% probability (i.e., 95% confidence interval). At 0.1C, the capacity SD is strongly influenced by the variation in particle radii, with the 30% variation reaching a capacity SD of around 2.5 Ah by almost 2000 cycles, in comparison to just 0.4 Ah at 10% variation, approximately. It should be noted that the capacity SD is similar across all % variation cases at BOL for 0.1C, but the gap between them widens with cycling. This can be attributed to the fact that the variation in the specific area available for electrochemical reactions across cells strongly influences SEI growth and thereby capacity loss. The other effects of variation in particle radii across cells, such as on diffusion length and surface overpotential, are less relevant at low C-rate. However, under the higher C-rate of 1C, the capacity SD remains almost stable and moderate, even at 30% variation. It plateaued below 1.5 Ah by approximately 1000 cycles, highlighting that the higher C-rate helps keep cells behaving in a more homogenous manner and suppressing cell-to-cell divergence. In fact, the capacity SD is much higher at BOL compared to 0.1C case and drops slightly. This suggests that the effect of particle radii variation on diffusion and kinetics, and thereby usable capacity, is more important than its effect of SEI growth, which is responsible for the slight reduction in capacity SD with cycling.

The set of plots in the second row, Fig.4(c-e), shows the spread of battery pack capacity over cycles. Similar to the capacity SD plots, the solid line in these plots shows mean pack capacity across the many runs performed using randomly drawn particle radii from the respective normal distributions for each run. The shaded region about the solid line shows the statistical spread of the outcome with a probability of 5% or more. At 0.1C, the statistical spread in pack capacity becomes larger with cycling, especially in the 30% case, where the spread widens by about 8 Ah near the end of life. At 1C, however, even at 30% variation, the spread remains narrow (i.e., 3–5 Ah), and the mean pack capacity stays close to the overall trend across all runs, reinforcing that a high C-rate during the operation seems to mitigate the stochastic effects of manufacturing differences. It should be noted that the simulations performed in the study included the assumption that SEI growth is the dominant degradation mechanism and, hence, these findings may not hold true if a different degradation mechanism were to be dominant in a particular cell type/chemistry using the set of operating conditions being considered in this study.
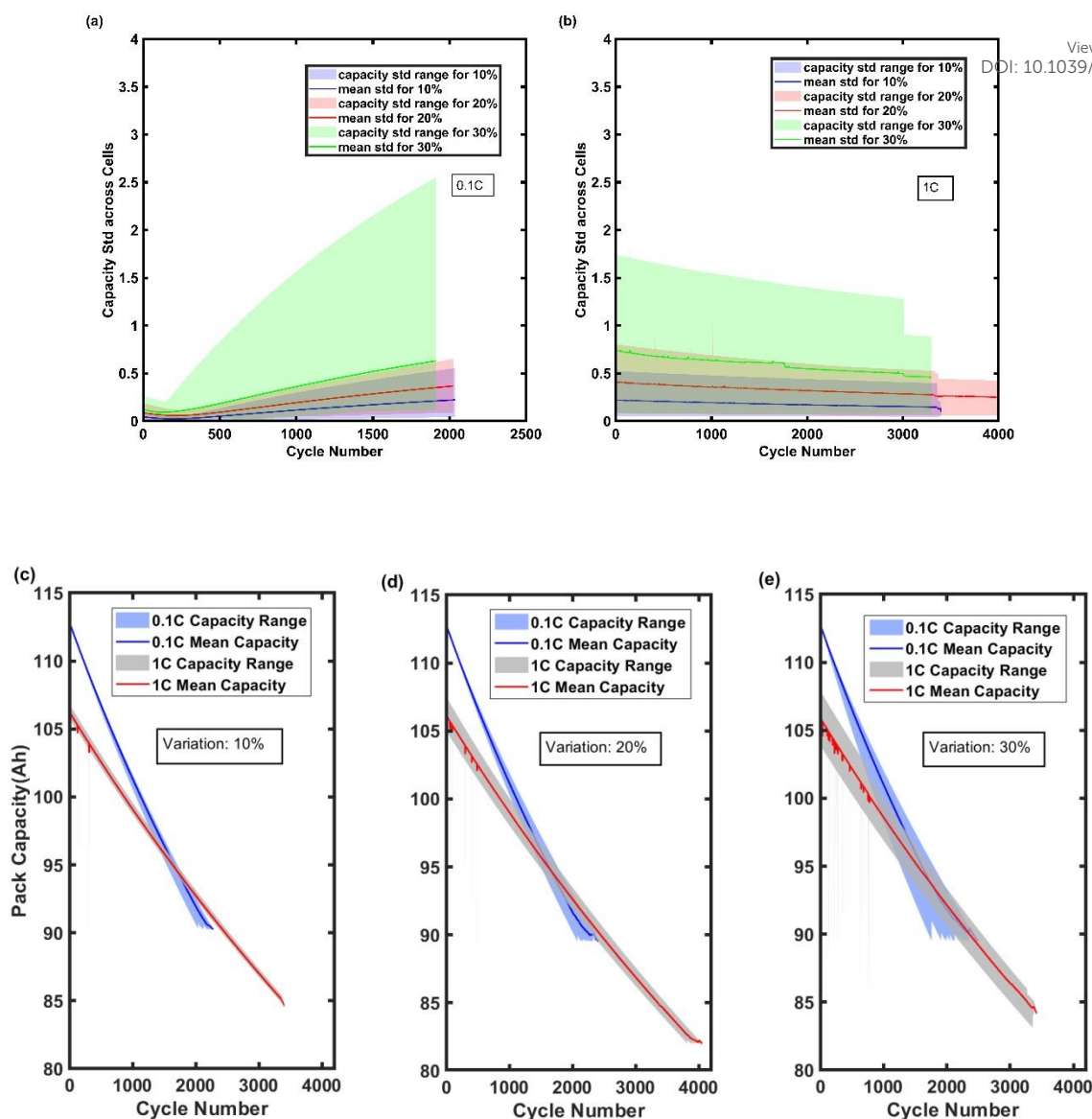
Fig. 4: Capacity analysis of 1S4P electrical configuration of battery pack. Panels (a, b): spread of capacity across cells at 0.1C and 1C, showing mean and standard deviation ranges for all three variation levels (i.e., 10%, 20%, 30%) over cycles. Panels (c-e): pack capacity degradation at 0.1C and 1C for 10%, 20%, and 30% capacity ranges over cycle life

All series electrical configuration—4S1P

The second case study involves a battery pack with a 4S1P electrical configuration cycled at two voltage windows, 2.75-4.2 V and 3.25-4 V, using the simulation methodology detailed previously. This case study is performed to understand how the variation in particle radius across cells operating at the same C-rate influences voltage divergence and how this ultimately affects the capacity fade trajectory at both the cell level and collectively as a pack.

As reflected in the data, for the 10% variation case, Cell 1 has the largest particle radius of 2.58 µm, while Cells 2, 3, and 4 have smaller particle radii, 1.55 µm, 1.49 µm, and 1.46 µm, respectively. According to Table 1, under a broader voltage window of 2.75-4.2 V, the initial capacity of the battery pack 27.8 Ah, approximately, drops below 22.3 Ah after 2847 cycles. Under a narrower voltage window of 3.25-4 V, the cycle life extended to 3918 cycles, with the pack capacity dropping from around 17.9 Ah to below 14.4 Ah. For the 20% variation case, Cell 2 has the largest particle radius of 3.12 µm, while Cells 1, 3, and 4 have particle radii of 1.04 µm, 1.2 µm, and 0.997 µm, respectively, resulting in 2667 cycles under the broader voltage window and 3510 cycles under the narrower voltage window of 3.25–4.0 V. The most extreme heterogeneous behavior is observed for the 30% variation case, where Cell 4 with the largest particle radius (3.59 µm) and Cells 1 to 3 having smaller radii of 0.3 µm, 0.22 µm, 0.62 µm, leading to the shortest cycle life: 1319 cycles under a voltage window of 2.75–4.2 V

and 1401 cycles under a voltage window of 3.25-4 V. Based on the pack capacity analysis, the narrower voltage window of 3.25-4 V extended the cycle life by 37.6%, 31.6%, and 6.2% for the 10%, 20%, and 30% variation cases, respectively.

Fig. S4 shows the SEI thickness of individual cells over their cycle life. Based on this figure, the cells with larger particle radii consistently maintain the thickest SEI layer, especially under a broader voltage window of 2.75-4.2 V. However, according to Fig. 5, the same cells experience the least capacity loss through SEI formation during their lifetime. For the 30% variation case, under a broader voltage window, Cell 4 has the thickest SEI layer, as confirmed by Fig. S3 (i.e., approximately 143 nm after 1319 cycles), compared to Cells 1 to 3 with SEI thickness ranging from 23 nm to 36 nm. However, Fig. 5 indicates that Cell 4, which has the thickest SEI layer, experiences the least capacity loss of around 2.8 Ah after 1319 cycles, compared to the roughly 3.8 Ah to 6.2 Ah capacity loss in Cells 1 to 3, despite their thinner SEI layers. This observation revealed that the thicker SEI layer in cells with a larger particle radius result from limited surface area per volume, but this greater thickness cannot compensate for the smaller specific surface area. Total SEI growth in the cells with larger particle radii remains lower than in small-particle cells with larger specific surface areas. The same pattern can be observed at 10% and 20% variations. Regarding the narrower voltage window, the same pattern is observed; however, the voltage window of 3.25–4 V slows down SEI formation across all cells, thereby mitigating uneven aging and capacity loss. According to the observations, the overall capacity loss and the disparity in capacity loss across four cells under both voltage windows intensified as the particle radius variation increased from 10% to 30%.
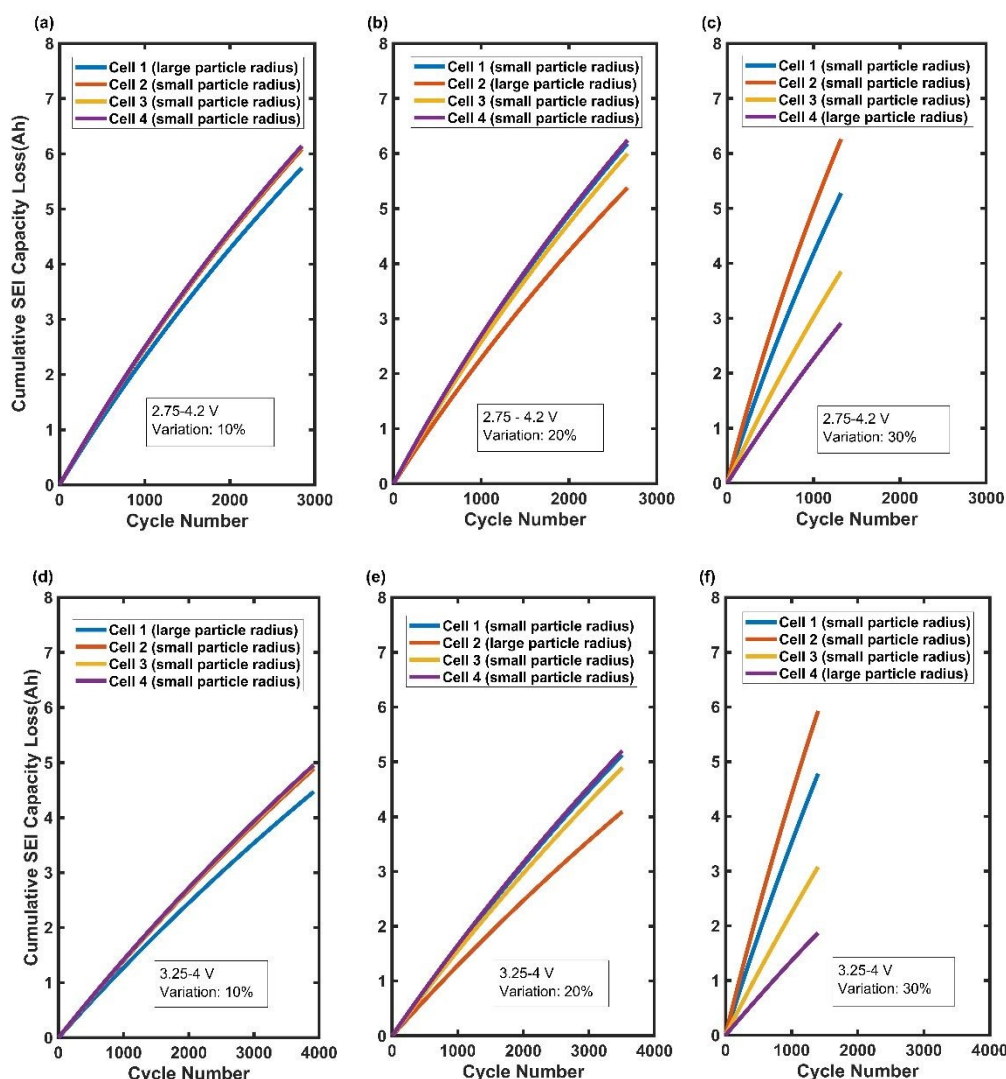
Fig. 5: Cumulative SEI capacity loss for four cells in the series connection. Plots compare capacity loss across cells over their cycle life at 1C, panels (a-c): under a voltage window of 2.75–4.2 V, panels (d-f): under a voltage window of 3.25-4 V.

Fig. 6 represents the voltage profiles at the BOL and EOL for the 10% and 30% variation cases under both voltage windows. At the BOL under the broader and narrower voltage windows, the voltage profile indicates a small difference across cells at the lowest variation of 10%. In comparison, there is a considerable divergence across cells' voltage profiles at the higher variability level of 30%. Under 2.75–4.2 V for the

30% variation case, the cell with the largest particle radius, Cell 4, discharged close to 2.1 V, which is significantly below the intended cell-level cut-off voltage of 2.75 V. During the charging phase, the same cell (i.e., Cell 4, with the largest particle radius) displayed higher voltage plateaus, reaching up to 4.3 V at the end of constant-current mode (CC) vs. approximately 4.15 V for the other three cells with smaller particle radii. The same trend was observed at a 10% variation, albeit with a smaller disparity across cells. This trend reversed as the pack reached the end of its life. At EOL, for the 30% variation case, the cell with the largest particle radius (i.e., Cell 4) only reach 3.3 V at the end of discharge, while the cells with a smaller particle radius over-discharged to around 2.1 V, becoming the most degraded member of the battery pack, thereby dictating the pack capacity. The narrower voltage window of 3.25-4 V minimized these effects, with the cell voltages not going below 3V at the end of discharge for all cases, and at EOL, only for the 30% variation, the cell with the thinnest SEI layer reached the end of discharge at around 2.95 V. In general, the narrower voltage window reduces voltage hysteresis and increases the cycle life of the battery pack for all three levels of variations compared to a broader voltage window. This occurs because of the battery operating over a broader voltage range, causing the electrodes to face more extreme conditions. As a result, the electrolyte breaks down more, making the SEI layer thicker and more complicated. While SEI growth is generally self-limiting, deep cycling in broad voltage ranges can cause repeated breakdown and regrowth. In contrast, narrower voltage windows reduce decomposition events, resulting in a lower rate of degradation.
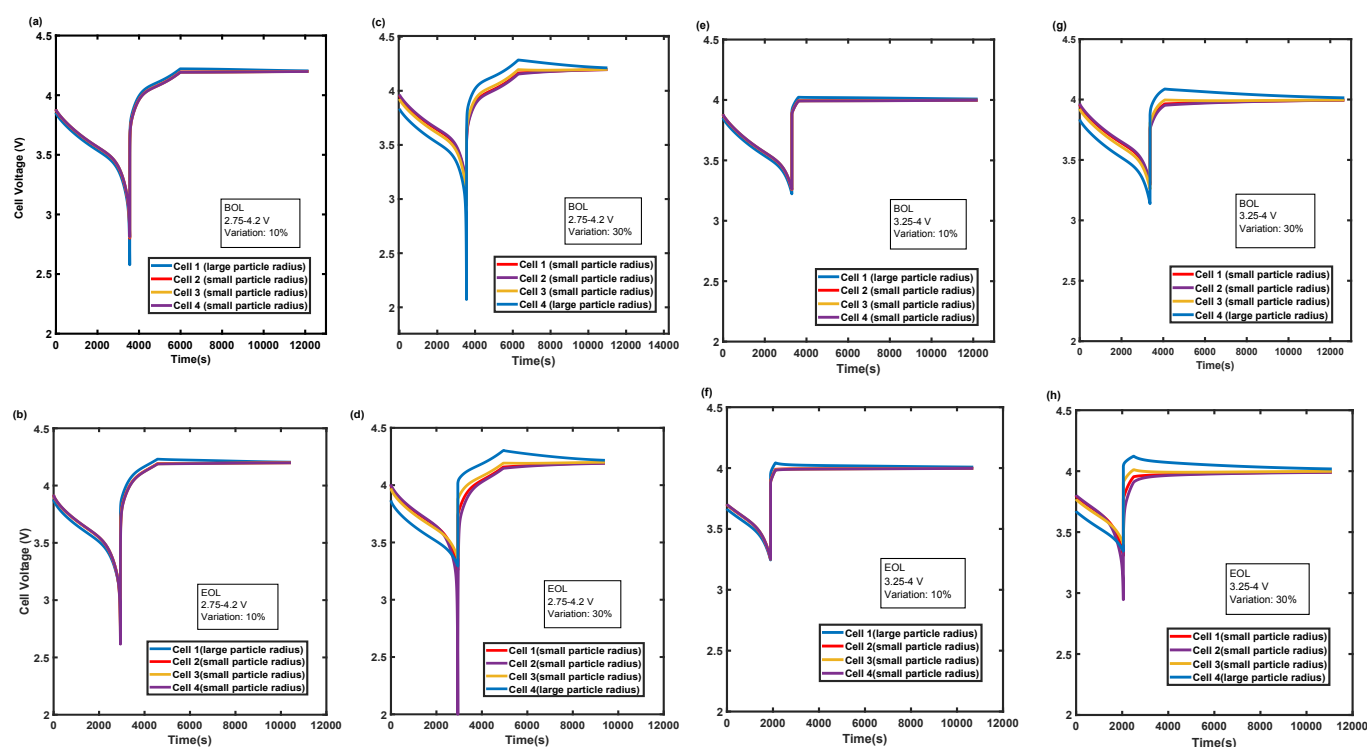

Fig. 6. Cell voltage profiles at BOL and EOL for a 4S1P configuration under varying particle radii and voltage windows. Panels (a–d) correspond to the BOL under both voltage windows, while panels (e–h) represent the EOL under both voltage windows.

It is worth mentioning the trend that is observed in the anode surface concentration to get a deep understanding of intercalation dynamics. All cells indicate similar sharp V-shaped concentration profiles at BOL, under both voltage windows. Regardless of the particle radius size and variability, all cells reach almost zero concentration at EOL and fully recover to the maximum concentration at the end of the charging phase at the same rate. However, at EOL, a significant disparity exists, especially in the 30% variation case. Under both voltage windows, the cells with a smaller particle radius exhibit a much lower surface concentration at the end of both the discharge and charging phases. This observation reveals that there is a substantial Lithium depletion as well as a reduction in intercalation efficiency over cycling. However, the cells with the largest particle radius maintain higher surface concentration at all times. This observation confirms that their lower specific surface areas protect them from substantial depletion over their cycle life. Moreover, based on the anode potential over time (Fig. S7) at BOL and EOL under 2.75–4.2 V, the cells with the largest particle radius, regardless of the level of variations, experience a larger downward shift in the anode potential by the end of CC-charge mode compared to cells with smaller particle radii. This is an indicator of higher resistance due to their thicker SEI layer. The same pattern is observed under a narrower voltage window of 3.25-4 V.

Fig.7 indicates the capacity spread generated from multiple simulation runs to provide a statistically meaningful assessment for the 4S1P case, of how random particle radius variation affects the cumulative SEI capacity loss across cells and the overall battery pack degradation. Fig. 7(a, b) indicates the cumulative SEI-induced capacity loss standard deviation (SD) over the cycle life of a battery pack. According to the

plots, the SD increases with cycling, reflecting the compounding divergence in SEI formation across the cells with various particle radii. As expected, the degree of spread becomes larger as the level of variation increases from 10% to 30%. For the 2.75–4.2 V case (Fig. 3a), the SD for the 30% variation case reaches almost 0.025 Ah after about 2200 cycles, while for the 10% variation case, it remains below 0.01 Ah even after 2800 cycles. Although the overall SEI loss is slightly lower, the same trend can be observed for the narrower voltage window of 3.25-4 V (Fig. 7b). These results suggest that the broader voltage window of 2.75-4.2 V accelerates cell degradation, thereby amplifying the effects of manufacturing differences. An increase in the SD would indicate that although the absolute capacity loss for each cell through SEI is small, the difference between the least degraded cells and the most degraded cells grows steadily over time, thereby reinforcing the risk of imbalance in long-cycle operation.

Fig. 7(c–e) presents the evolution of 4S1P-configuration pack capacity for 10%, 20%, and 30% variation, respectively. Each plot shows capacity trends under both voltage windows. According to the plots, the mean pack capacity degrades faster under a broader voltage window of 2.75–4.2 V across all three cases, due to the increased time spent at electrochemically active potentials that promote SEI growth. Another observation is that the statistical spread in a pack capacity increases with both cycle number and variation level. For the 30% case (Fig. 7e), the spread becomes significantly larger after around 2000 cycles, where the divergence between the top and bottom percentiles reaches 3 Ah. This divergence is particularly pronounced in the blue-shaded region (2.75–4.2 V), consistent with the stronger amplification of non-uniform degradation under more aggressive cycling conditions. The spread is more moderate under a narrower voltage window of 3.25–4.0 V, and the pack capacity spread converges over cycling, but still a non-negligible range is observed, indicating that cell-to-cell variation has a long-term influence on pack performance regardless of the voltage window. It is important to note that the 4S1P configuration exacerbates the consequences of variation, since the weakest cell dictates the pack capacity. Therefore, even small differences in the physical properties of the cells might lead to significant uneven aging of the battery pack and its overall aging rate. These findings reinforce that in series-dominant architectures like 4S1P, the combination of broader voltage windows, high variation in the particle radius, and long cycle life can increase the level of uneven aging. The use of a narrower voltage window or smaller manufacturing variation level in the cells' particle radius can help suppress this divergence.
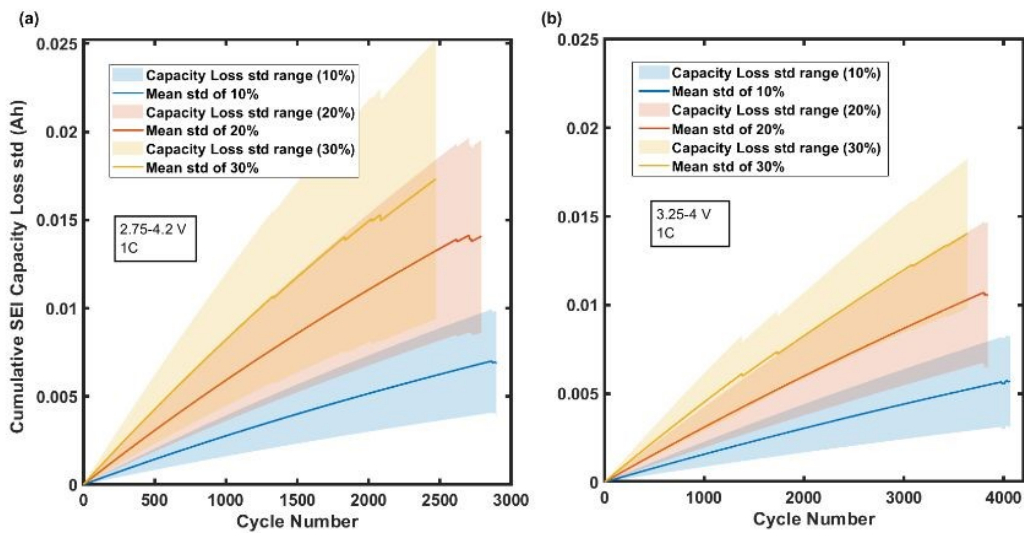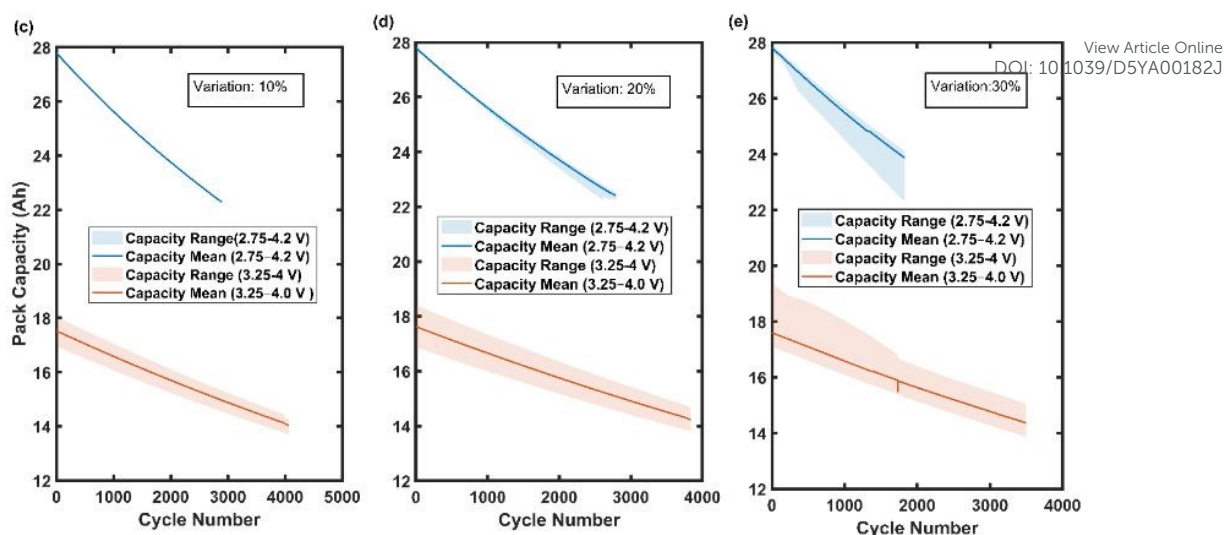
Fig. 7: Capacity Analysis of Series-Connected Cells. Panels (a, b): Spread of cumulative SEI capacity loss across cells under 2.75-4.2 V and 3.25-4 V; panels (c-e) show the degradation of pack capacity under both voltage windows for 10%, 20%, and 30% variation, respectively.

Series-parallel electrical configuration - 2S2P

The last case study involves a battery pack with a 2S2P electrical configuration cycled at two C-rates: 0.1C and 1C under broader and narrower voltage windows of 2.75-4.2 V and 3.25-4 V, respectively. According to the data, the higher particle radius variations (e.g., 30%) significantly shorten cycle life, particularly at a lower C-rate of 0.1C, where uneven aging is more pronounced. The cycle life consistently diminishes across all combinations of operating conditions as the particle radius variation escalates from 10% to 30%. The decline in cycle life is more significant at the lower C-rate of 0.1C, where uneven aging caused by SEI degradation mechanism becomes more severe. For instance, for the 30% variation case at 0.1C and broader voltage window, the cycle life significantly decreases to 815 cycles, compared to 2021 cycles for the 10% variation case (Table 1). Furthermore, cycling under a narrower voltage window alleviates the impact of uneven aging, resulting in a significant improvement in cycle life irrespective of the C-rate. However, the influence of the voltage window proved to be less effective as the particle radius variation increased. As mentioned earlier, the modeling framework used in this study only accounts for SEI growth as the degradation mechanism. Consequently, alternative aging mechanisms, such as lithium plating and particle cracking, which are recognized to become prominent at elevated C-rates, are not present in this model. Hence, the model may underestimate aging at high C-rates. The conclusions derived are consequently restricted to SEI-driven aging trends, which seem to be more susceptible to uneven aging at lower C-rates.

Cell capacity trends over time, as shown in Fig. 8 and Fig. 9, clearly demonstrate the impact of particle radius variation on uneven aging under different operating conditions. Across all conditions, cells with a smaller particle radius consistently exhibited greater capacity loss due to their larger specific surface area, which is available for side reactions. The effect is particularly pronounced at the lower C-rate of 0.1C, where capacity divergence between cells becomes more severe as cycling progresses. For the 30% variation case, Cell 1 and Cell 2, with particle radii of 3.49 μm and 3.77 μm, at 0.1C under 2.75–4.2 V faded from 28.1 Ah to 26.1 Ah, approximately, resulting in around 2 Ah capacity loss over cycles at a rate of approximately 2.48 mAh/cycle. Cell 3 and Cell 4, with the smallest particle radii of 0.68 μm and 0.29 μm, faded from approximately 28.3 Ah to 19.9 Ah, an 8.44 Ah loss at rate of approximately 10.36 mAh/cycle. At 1C and under 3.25–4.0 V, Cell 1 and Cell 2 experienced capacity loss of around 1.2 mAh per cycle, while Cell 3 and Cell 4 experienced capacity loss of around 2.7 mAh per cycle. In contrast, one of the least severe cases occurs in the 10% variation case at 1C under the narrower voltage window, where Cell 3 and Cell 4 with the largest particle radii lost roughly 2.6 Ah at a rate close to 0.7 mAh/cycle, while Cell 1 and Cell 2 with the smallest particle radii lost approximately 3.7 Ah at a rate slightly over 0.9 mAh/cycle, which amounted to a 44.0% greater capacity loss for Cell 1 and Cell 2. At the 10% variation scenario, the capacity loss is significantly smaller compared to the 30% variation scenario, and the gap between the cells remains relatively limited. Furthermore, at a higher C-rate of 1C, regardless of the variation level, there was a significant difference between the initial capacity of the cells. However, over their cycle life, this difference diminished. In contrast, the opposite behavior was observed at a lower C-rate of 0.1C, where cells' capacity diverged more as they cycled, confirmed by Fig. 8(a-c) and Fig. 9(a-c). At 1C, especially under a narrower voltage window of 3.25-4, Fig. 9(d-f), the capacity of the cells with a larger particle radius is always considerably lower than the cells with a smaller particle radius due to less available specific surface area for the intercalation of the lithium ions in the larger-particle cells. Regarding the effect of voltage windows on degradation rate, a broader voltage window resulted in a faster degradation rate, indicating that deeper degrees of lithiation and delithiation of the electrodes intensified the degradation.
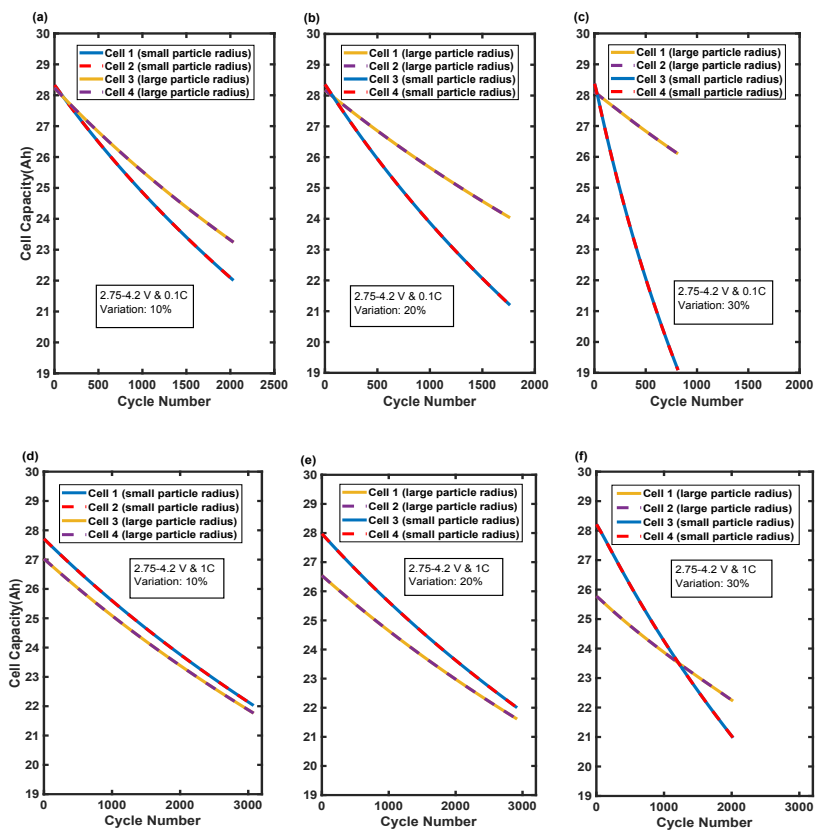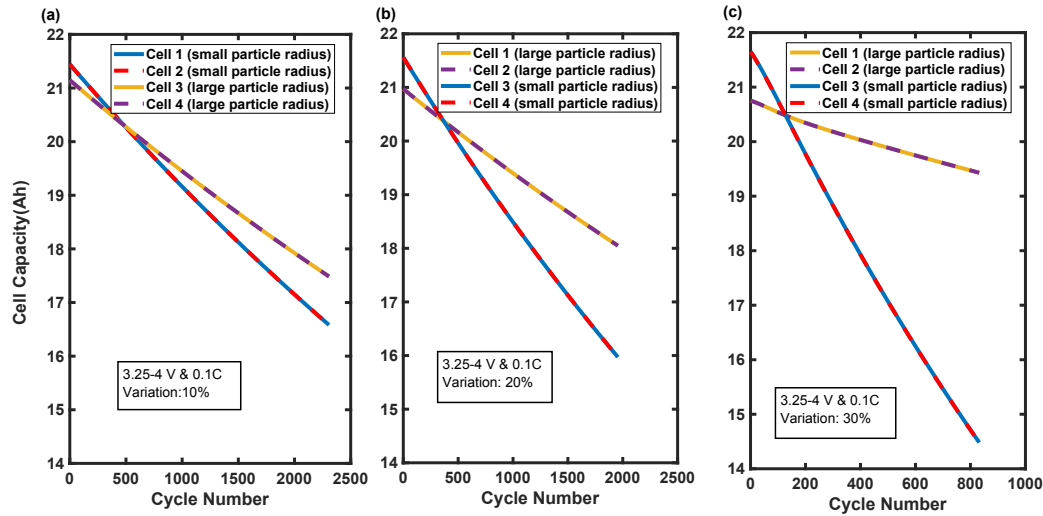
Fig. 8: Evolution of individual cell capacities at various manufacturing variation levels, for the 2S2P configuration under voltage window of 2.75-4.2 V. Panels (a-c) show results at 0.1C; panels (d-f) show the results at 1C.
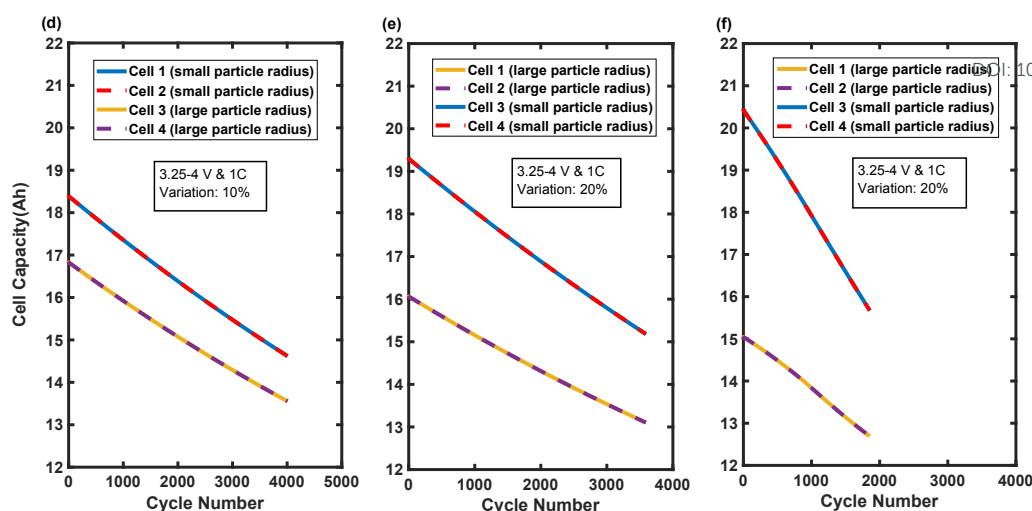
Fig. 9: Evolution of individual cell capacities at various manufacturing variation levels, for the 2S2P configuration under voltage window of 3.25-4 V. Panels (a-c) show results at 0.1C; panels (d-f) show the results at 1C.

Fig. S11 indicates the SEI growth over time in all cases. For the 10% variation case at 0.1C under 2.75–4.2 V, Cell 3's SEI layer grew to 178 nm, while Cell 2 reached 136 nm, despite the higher capacity fade of Cell 2. For the 20% variation case, at 0.1C under 2.75–4.2 V, Cell 1's SEI layer grew to 180 nm, while Cell 3 reached 105 nm, yet Cell 3 experienced 72.8% greater capacity loss. One reason behind this phenomenon is that the cells with a larger particle radius develop a thicker SEI layer but not more SEI growth, because the interface area over which SEI is spread is less than the cells with a smaller particle radius. In contrast, cells with smaller particle radii possess a much higher surface area, resulting in the SEI layer being thinner, yet the total volume of SEI is larger, consuming more lithium and leading to greater capacity loss. For the 30% variation case at 0.1C under 2.75–4.2 V, Cell 1's SEI layer grew to 103 nm, while Cell 3 reached 54.9 nm, with Cell 3, according to Fig. 6, experiencing considerably greater capacity loss, reflecting its higher surface area's susceptibility to SEI formation over time. The same trend is observed under the other operating conditions for three different levels of variation. According to the observation, cells with larger particle radii show a thicker SEI layer all the time, but their thicker SEI layer is not large enough to make up for the lesser specific surface area compared to cells with smaller particle radii.

Voltage and scaled current profiles, Fig. 10 and Fig. 11, provide further insight into uneven aging. At end of life (EOL), the voltage profiles across all levels of variation (i.e., 10% and 30%) reveal distinct patterns of divergence that were not seen at the beginning of life (BOL). While BOL indicates overlapping voltage profiles across the four cells, the EOL plots clearly indicate the effect of cell-to-cell variations on the voltage profiles of each individual cell by indicating the voltage separation, particularly under the 30% variation condition, Fig. 10(d) and Fig. 11(h). This separation indicates that uneven aging has progressed, with some cells experiencing lower voltage cut-offs, revealing their higher internal resistance or lower remaining capacity. According to Fig. 10, at EOL for the 10% variation case, scaled current profiles during discharge indicate that Cell 3 and Cell 4, the cells with larger particle radii and belonging to the string with lesser degradation, deliver slightly more current than the nominal current (i.e., 1.1-1.2 × nominal current), while Cell 1 and Cell 2 , the cells with smaller particle radii and belonging to the string with higher degradation, deliver lesser than the nominal current (i.e.,0.8-0.9 x nominal current). At 30% variations, the roles reverse, Cell 1 and Cell 2 deliver more current than the nominal current (i.e., 1.3–1.5×nominal current), while Cell 3 and Cell 4 deliver lesser than the nominal current (i.e., 0.6–0.8 x nominal current). This behavior arises because both cells must carry the same current in a series string, and the overall string contribution to the pack current depends on the combined health of the two cells. A degraded string effectively becomes the "weak link," unable to sustain ideal discharge current, forcing the healthier string to compensate by carrying a disproportionate share. At 1C, these effects become even more pronounced. The operation under higher current rate amplifies kinetic limitations, causing stronger current deviations between strings. For example, for the 30% variation case at 1C under a broader voltage window of 2.75-4.2 V, as shown in Fig. 10, the healthier string's current deviation rises to about 1.7–2.0, while the degraded string's current deviation dropped below 0.5 relative to the nominal current. Moreover, according to Fig. 8(f), Cell 3 and Cell 4, the two cells with a smaller particle radius, indicate higher initial capacities compared to Cell 1 and Cell 2, with a larger particle radius. The higher capacities arise from more available specific surface area, enhancing the intercalation kinetics, and lower diffusion limitation due to the shorter diffusion length. However, these cells degraded at a higher rate over their life due to higher loss of Lithium inventory (LLI). The capacity curves of the smaller-particle cells intersect with the capacity curves of the larger-particle cells at approximately 1000 cycles, and after this intersection, the capacity of Cell 3 and Cell 4 continued to fade more steeply. Under the same operating conditions, such behavior is not observed at a lower

variation case (i.e., 10% and 20%). Furthermore, Cell 4 exhibits the thinnest SEI layer among all cells over the cycle life of the battery pack, while it has the highest rate of capacity fade, due to a larger specific surface area. Cell 4 operates at a higher anode potential during the charging phase, as shown in Fig. S10. This suggests that SEI formation is suppressed due to slowed kinetics at elevated potentials. Despite the thin SEI, the dominant degradation mechanism in Cell 4 appears to be LLI. This is likely caused by irreversible Lithium consumption through over-lithiation in the early cycles or imbalance-driven over-discharge during extended cycling, as confirmed by Fig. 10(d) which represents the voltage profile of all four cells at EOL.
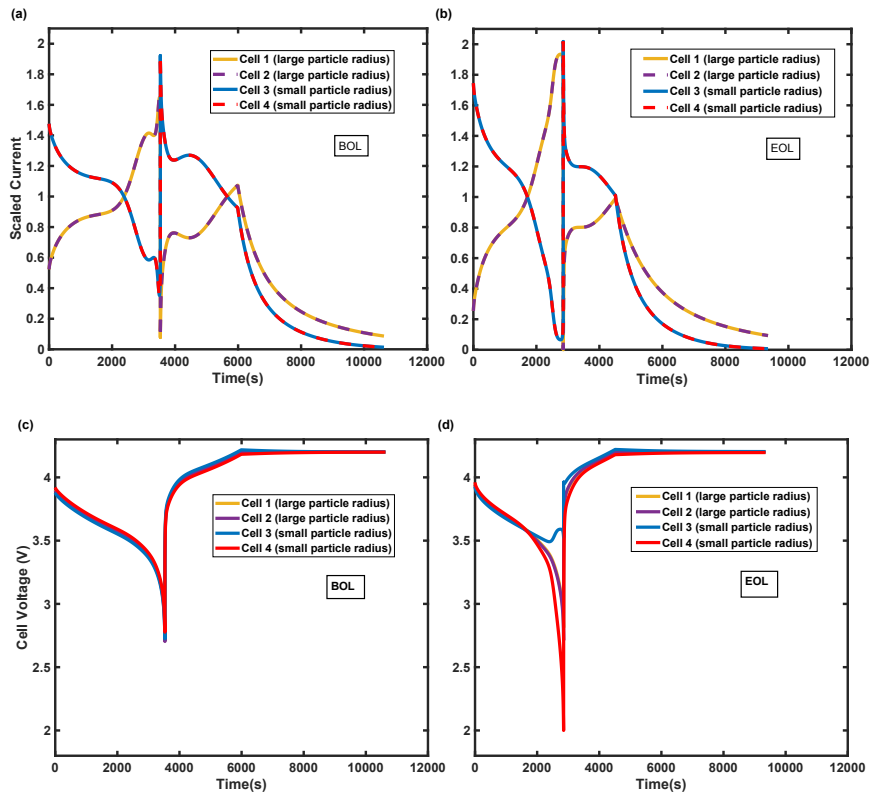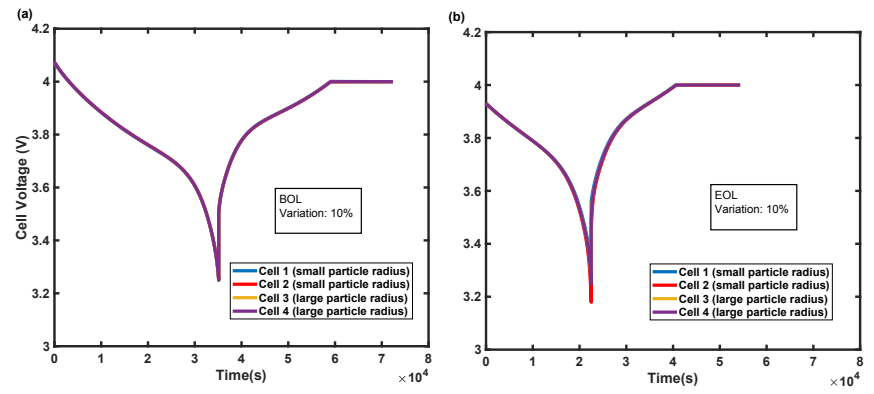
Fig. 10: Scaled current and cells' voltage profiles in a 2S2P battery pack with 30% particle radius variation, cycled at 1C under 2.75–4.2 V. Panels (a, c) show the beginning of life (BOL) scaled current and voltage responses, while panels (b, d) correspond to end of life (EOL).
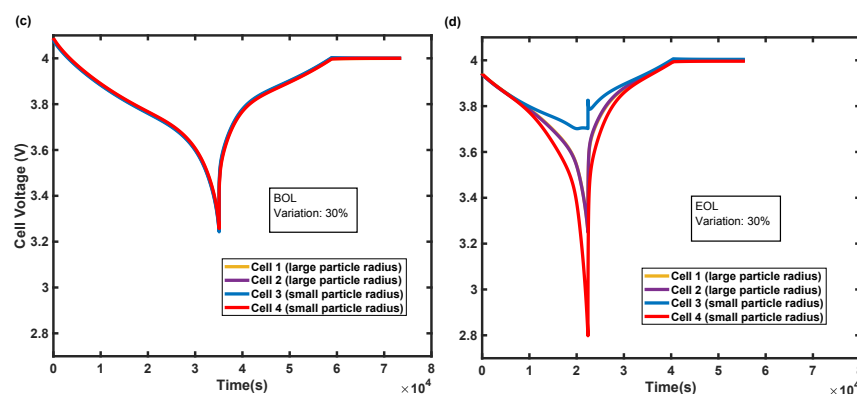
Fig. 11: Cell voltage profiles for four cells in a battery pack with a 2S2P electrical configuration for 10% and 30% particle radius variation, cycled at 0.1C under 3.25–4.0 V. Panels (a, b) display the BOL and EOL voltage profiles, respectively, for the 10% variation case. Panels (c, d) display the corresponding BOL and EOL voltage profiles for the 30% variation case

Fig. 12(a–d) indicates the evolution of the cells' capacity standard deviation (SD) in a battery pack with a 2S2P electrical configuration subjected to three different particle radius variations (i.e., 10%, 20%, 30%). Each scenario is simulated across multiple Monte Carlo runs, repeated until the SEM reached a threshold of 5%, ensuring a statistically reliable data set. At 0.1C and 2.75–4.2 V, Fig. 12(a), capacity SD indicates a growing divergence over their cycle life, with a more severity at a 30% particle radius variation. The capacity SD for a 10% and 20% particle radius variation remains below 0.6 Ah and 0.25 Ah by approximately 1500 and 2000 cycles, respectively; while by 1000 cycles, the capacity SD for the 30% variation is ~2 Ah. This observation indicates that at low C-rates, even small deviations in microstructural properties like particle radius can considerably exacerbate uneven aging due to differences in the available specific surface area which leads to vastly different rates of SEI growth among cells. In contrast, at 1C and 2.75–4.2 V, Fig. 12(b), across all levels of variation, capacity SD remains low and decreases gradually. The highest SD belongs to a 30% variation case, and it remains under 0.6 Ah over the cycle life. The same behavior observed under a narrower voltage window of 3.25–4.0 V, but with lower absolute capacity SD values. For instance, at 0.1C, Fig. 12(c), the 30% variation leads to a growing SD, reaching roughly 1 Ah by 1500 cycles, but it remains significantly lower than in a broader voltage window of 2.75-4.2 V, Fig.12(a). This suggests that restricting the voltage window limits SEI-related degradation and delays divergence. Under 1C and 3.25–4.0 V operating condition, Fig. 12(d), capacity SD range indicates a higher deviation compared to the simulations under the same C-rate but a broader voltage window. Whereas the 10% case stays within around 0.6 Ah at EOL, the 30% variance case shows roughly 1.5 Ah by EOL. (i.e., approximately 4000 cycles). High C-rate and a smaller voltage window resulted in a longer cycle life that reflected a more consistent deterioration pattern over the pack's cells.

Figs. 12(e–g) indicate the evolution of pack capacity and its statistical spread across multiple simulation runs. At 10% variation, the pack capacity remains consistent across runs, with a marginal spread under all operating conditions. However, for 20% and 30% variations, the spread increases, notably at 0.1C under 2.75–4.2 V operating condition (e.g., in the 30% variation case, reached roughly 9 Ah after 1000 cycles). In contrast, operating under a higher C-rate of 1C consistently restricts the capacity spread, particularly when it is combined with a narrower voltage window of 3.25-4 V, where capacity degradation is minimized. This indicates that elevated C-rates and a narrower voltage window may alleviate the effects of manufacturing discrepancies, leading to a more uniform pack behavior despite the presence of variability in particle radius.

(a)

(b)

(c)

(d)

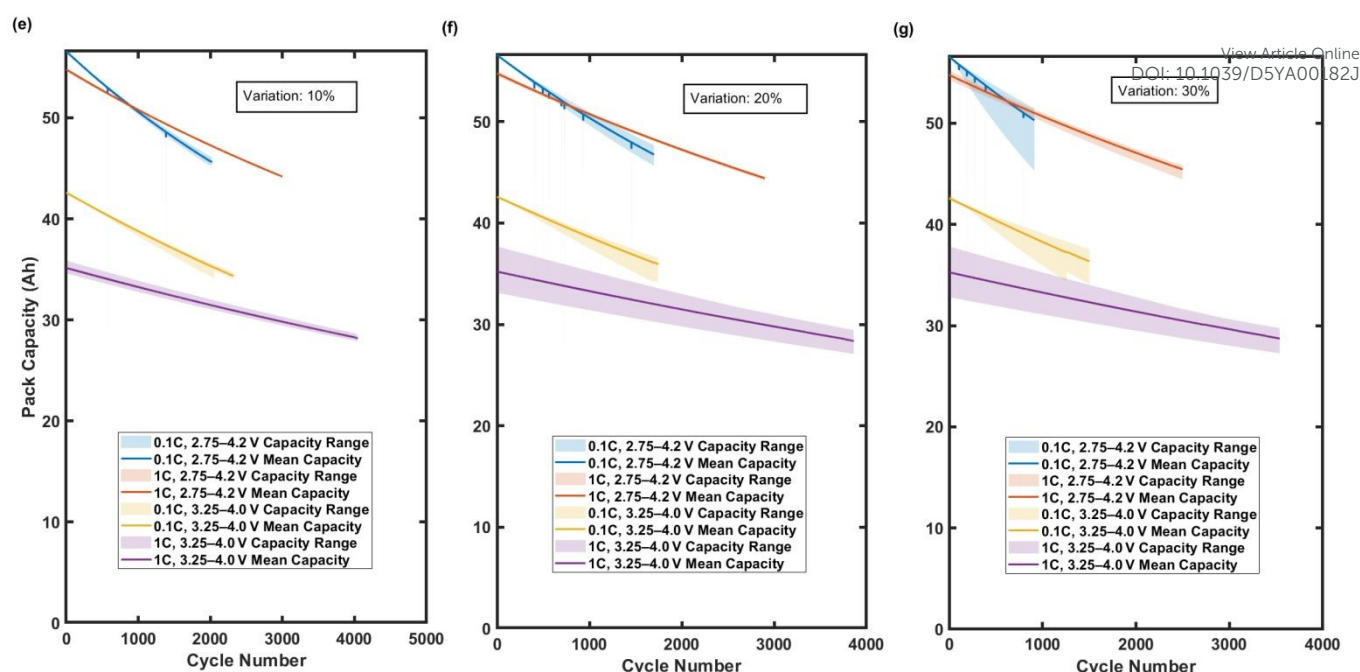**Energy Advances Accepted Manuscript**
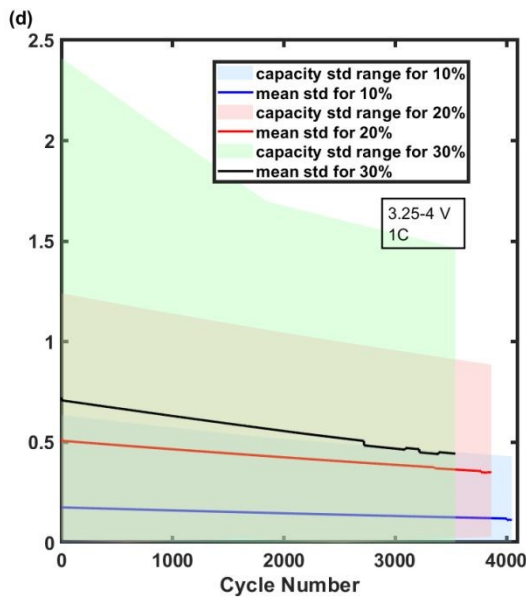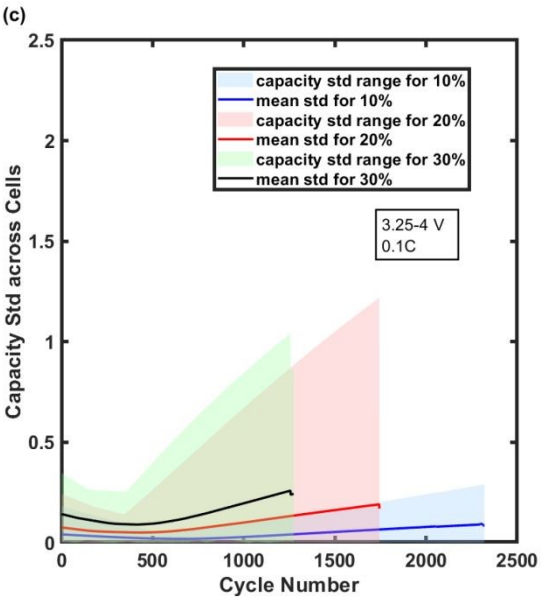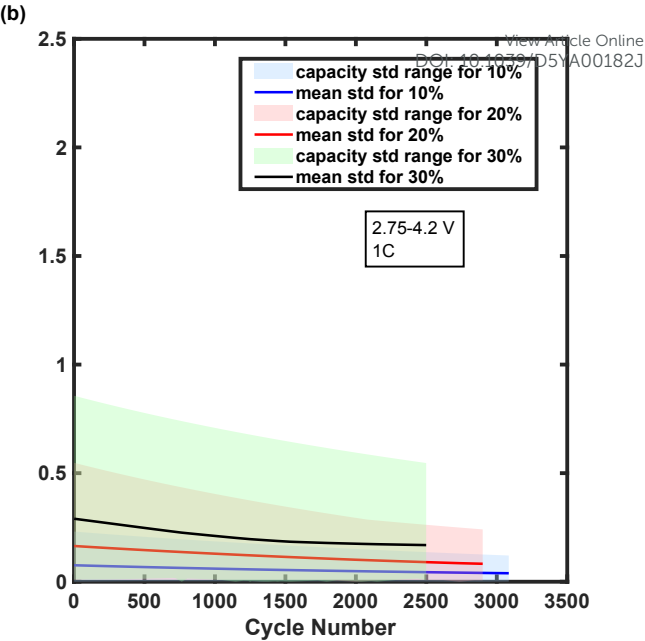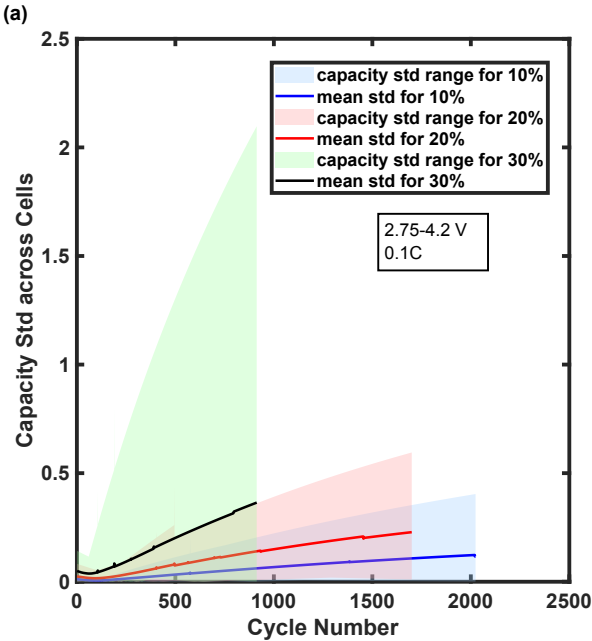
Fig. 12. Capacity standard deviation (SD) across cells and pack capacity evolution for a 2S2P battery pack under three levels of particle radius variation: 10%, 20%, and 30%. Four operating conditions were tested: 0.1C and 1C under voltage windows of 2.75–4.2 V and 3.25–4.0 Panels (a–d) display the cells' capacity spread (SD) across cycles within the pack. Panels (e–g) display the corresponding pack capacity and its statistical spread across cycles

Scaling of Uneven Aging and Parallel Averaging Effects:

To evaluate how uneven aging scales with pack size, we computed the standard deviation (STD) of per-cell percent capacity fade for five configurations—2S2P (4 cells), 3S3P (9), 4S4P (16), 5S5P (25), and 7S7P (49)—operated under identical conditions (0.1 C, 2.75–4.20 V). Uneven aging was quantified as the per-cycle growth rate of the standard deviation (STD) of per-cell capacity fade (%), estimated from the slope of STD versus cycle (Fig. 13). The resulting trend was non-monotonic: the 2S2P pack exhibited the lowest unevenness rate, the 3S3P and 4S4P packs showed higher unevenness rates, and the 5S5P and 7S7P packs declined again. This pattern is consistent with competing mechanisms: series connections accentuate weakest-cell bottlenecks (amplifying divergence), whereas parallel branches partially average cell-to-cell variability (damping divergence). Random placement of particles with larger/smaller radii among parallel branches further modulated the net effect, precluding simple proportional scaling with total cell count. Table 2 summarizes all discussed information.

Table 2. Uneven-aging rate and cycle life to 80% pack capacity for different pack sizes.

Configuration	Cells	Uneven-aging rate (ΔSTD per cycle, %)	EOL (Cycles to 80%)
2S2P	4	0.0104	1140
3S3P	9	0.0213	326
4S4P	16	0.0216	305
5S5P	25	0.0170	298
7S7P	49	0.0165	281

Pack end-of-life (EOL, 80% capacity) corroborated these observations (Fig. 14). EOL dropped sharply when moving from 2S2P to 3S3P but then decreased more gradually with larger packs, and a linear regression of EOL versus pack size yielded a slope whose confidence interval crossed zero—indicating no statistically significant monotonic scaling of life with cell count. Collectively, these results suggest that increasing series count primarily governs the bottleneck behavior, while added parallelization provides partial mitigation via averaging. The combined

evidence from the STD-growth metric and EOL analysis thus supports our interpretation that uneven aging does not scale linearly with pack size but rather reflects the balance between series-imposed constraints and parallel averaging.
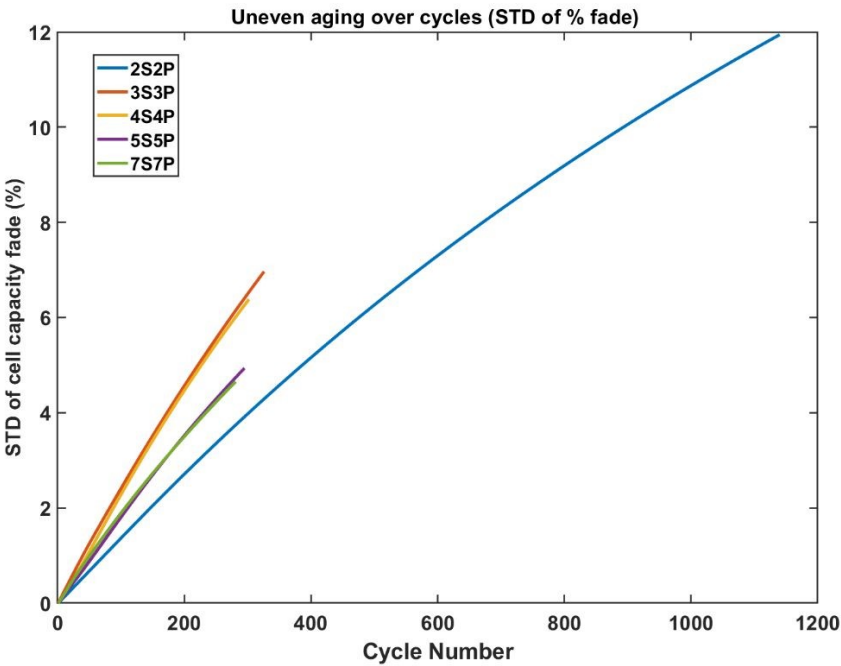
Fig. 13. Evolution of uneven aging with cycling for different pack configurations (2S2P–7S7P). The plot shows the standard deviation (STD) of per-cell capacity fade (%) as a function of cycle number, quantifying the extent of nonuniform degradation within each pack.
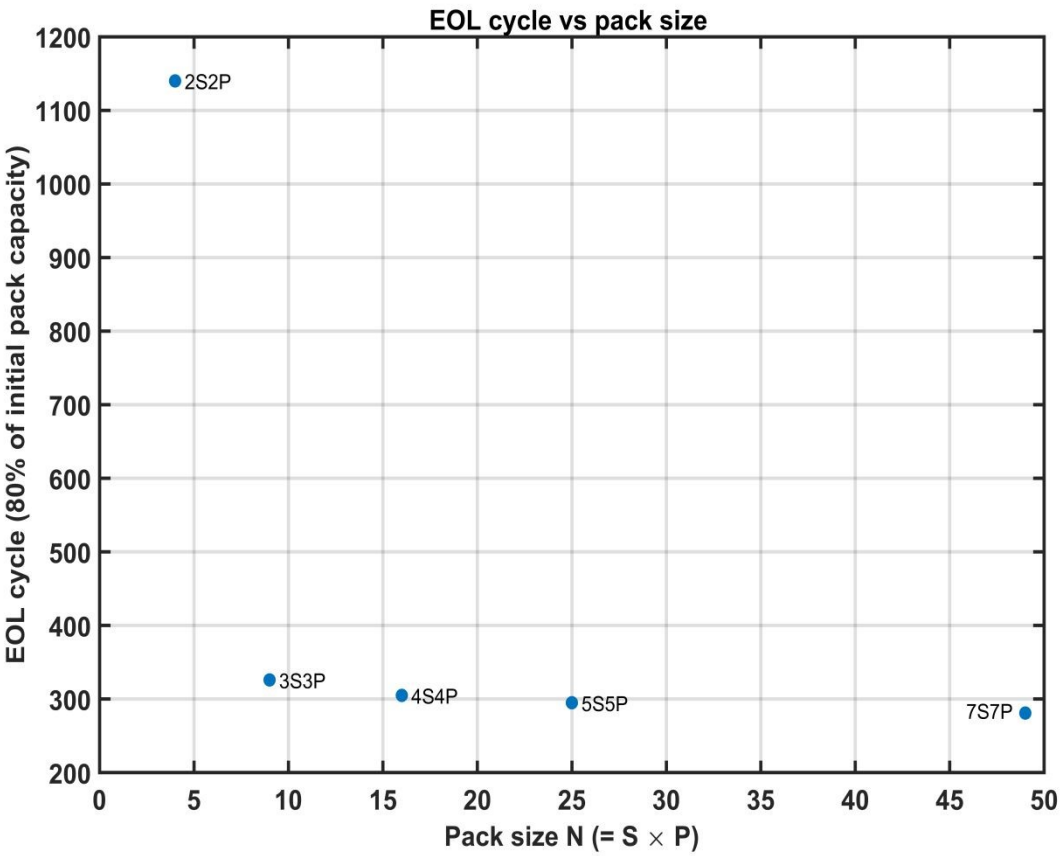
Fig. 14. End-of-life (EOL) cycle number versus pack size for configurations ranging from 2S2P to 7S7P. The EOL was defined as the cycle number corresponding to 80% of the initial pack capacity.

Conclusion:

This study highlights the critical challenge of uneven aging in Lithium-ion battery packs, where variations in degradation rates among cells can lead to performance losses, safety risks, and reduced lifespan. While previous studies have focused on differences in cell resistance and capacity as contributors to this phenomenon, this work quantifies the effect of material-level variations, in particular active material particle size, on the cell- and pack-level aging characteristics. By incorporating SEI growth as a degradation mechanism in an electrochemical battery model, the study shows that even a small variation in the particle radius can lead to considerable disparities in capacity fade among cells, ultimately affecting the pack's overall degradation trajectory. The results demonstrate that uneven aging is influenced not only by electrical configuration (i.e., series, parallel, and combined) but also by operating conditions such as C-rate and voltage window. Notably, lower C-rates and broader voltage windows exacerbate divergence in aging, while higher C-rates appear to suppress variation due to the effect of particle size on charge transfer kinetics. The novelty of this work lies in tracing uneven pack-level aging back to microstructural origins, connecting cell- and pack-level aging behavior to the internal states of the battery, and providing insights into effective cell and pack manufacturing.

References:

1 L. Gaines, K. Richa and J. Spangenberger, Key issues for Li-ion battery recycling, MRS Energy Sustain., 2018, 5, 13, 1–14, DOI: 10.1557/mre.2018.13.

2 M. A. Hannan, M. M. Hoque, A. Hussain, Y. Yusof and P. J. Ker, State-of-the-art and energy management system of lithium-ion batteries in electric vehicle applications: issues and recommendations, IEEE Access, 2018, 6, 19362–19378, DOI: 10.1109/ACCESS.2018.2817655.

3 T. Horiba, Lithium-ion battery systems, Proc. IEEE, 2014, 102, 6, 939–950, DOI: 10.1109/JPROC.2014.2313733.

4 X. Liu, K. Li and X. Li, The electrochemical performance and applications of several popular lithium-ion batteries for electric vehicles – a review, Commun. Comput. Inf. Sci., 2018, 892, 19–34, DOI: 10.1007/978-981-13-2381-2_19.

5 T. Wulandari, D. Fawcett, S. B. Majumder and G. E. J. Poinern, Lithium-based batteries: history, current status, challenges, and future perspectives, Batter. Energy, 2023, 2, 1–15, DOI: 10.1002/bte2.20230030.

6 D. Galatro, D. A. Romero, J. A. Freitez, C. Da Silva, O. Trescases and C. H. Amon, Modeling degradation of lithium-ion batteries considering cell-to-cell variations, J. Energy Storage, 2023, 62, 106011, DOI: 10.1016/j.est.2023.106011.

7 X. Feng, M. Ouyang, X. Liu, L. Lu, Y. Xia and X. He, Thermal runaway mechanism of lithium-ion battery for electric vehicles: a review, Energy Storage Mater., 2018, 10, 246–267, DOI: 10.1016/j.ensm.2018.09.009.

8 B. Klayman and W. Bernie, Tesla reports third fire involving Model S electric car, Reuters, 2013.

9 M. Baumann, L. Wildfeuer, S. Rohr and M. Lienkamp, Parameter variations within Li-ion battery packs – theoretical investigations and experimental quantification, J. Energy Storage, 2018, 18, 295–307, DOI: 10.1016/j.est.2018.05.023.

10 H. He and X. Chen, Analysing unbalanced ageing in EV battery packs using the low-cost lumped single particle model (LSPM): the impact of temperature gradients among parallel-connected cells, Transp. Res. Procedia, 2023, 70, 406–413.

11 S. F. Schuster, M. J. Brand, P. Berg, M. Gleissenberger and A. Jossen, Lithium-ion cell-to-cell variation during battery electric vehicle operation, J. Power Sources, 2015, 297, 242–251.

12 Y. Lee, J. Park and W. Lu, A comprehensive experimental and modeling study on dissolution in Li-ion batteries, J. Electrochem. Soc., 2019, 166, 7, A1193–A1202.

13 R. Gailani, R. Mokidm, M. Al-Greer et al., Analysis of lithium-ion battery cells degradation based on different manufacturers, Proc. Int. Univ. Power Eng. Conf. (UPEC), 2020, 1–6, DOI: 10.1109/UPEC49904.2020.9209759.

14 L. Wildfeuer, A. Karger, M. Lienkamp et al., Experimental degradation study of a commercial lithium-ion battery, J. Power Sources, 2023, 543, 232498, DOI: 10.1016/j.jpowsour.2022.232498.

15 G. M. Trippetta, Y. Fang, A. Siddiqui, R. Lindstrom, G. Lindbergh and H. Ekström, Methods for characterization of heterogeneous aging in large lithium-ion batteries, ECS Meet. Abstr., 2023.

16 G. Sordi, C. Rabissi and A. Casalegno, Understanding lithium-ion battery degradation through P2D model parameters evolution, ECS Meet. Abstr., 2023.

17 X. Zhang, S. Chumakov, X. Li, M. Klinsmann, S. U. Kim, C. R. Linder and J. Christensen, An electro-chemo-thermo-mechanical coupled three-dimensional computational framework for lithium-ion batteries, J. Electrochem. Soc., 2020.

18 A. Allam and S. Onori, Exploring the dependence of cell aging dynamics on thermal gradient in battery modules: a PDE-based time scale separation approach, Proc. Eur. Control Conf. (ECC), 2019, 1–6.

19 F. A. Lebel, P. Messier, A. Tessier and J. Trovão, Implications of lithium-ion cell variations on multi-cell battery pack thermal runaway, Proc. Veh. Power Propuls. Conf., 2019, 5–12.

20 I. Zilberman, S. Ludwig and A. Jossen, Online aging determination in lithium-ion battery module with forced temperature gradient, J. Energy Storage, 2020, 27, 101170, DOI: 10.1016/j.est.2019.101170.

21 M. Loveridge, G. Remy, N. Kourra et al., Looking deeper into the Galaxy (Note 7), Batteries, 2018, 4, 3.

22 G. Zhao, X. Wang and M. Negnevitsky, Connecting battery technologies for electric vehicles from battery materials to management, iScience, 2022, 25, 2, 103744.

23 M. S. Hosen, P. Yadav, J. Van Mierlo and M. Berecibar, A post-mortem study case of a dynamically aged commercial NMC cell, Energies, 2023, 16, 4, 1046, DOI: 10.3390/en16031046.

24 Y. Olofsson, J. Groot, T. Katrašnik and G. Tavčar, Impedance spectroscopy characterization of automotive NMC/graphite Li-ion cells aged with realistic PHEV load profile: quantification of cell properties vs. temperature at different stages of ageing, Volvo GTT, Advanced Technology & Research, Göteborg, Sweden, and University of Ljubljana, Faculty of Mechanical Engineering, Ljubljana, Slovenia, 2023.

25 I. Buchberger, S. Seidlmayer, A. Pokharel, M. Piana, J. Hattendorff, P. Kudejova, R. Gilles and H. A. Gasteiger, Aging analysis of graphite/$LiNi_{1/3}Mn_{1/3}Co_{1/3}O_2$ cells using XRD, PGAA, and AC impedance, J. Electrochem. Soc., 2015, 162, 14, A2737–A2746, DOI: 10.1149/2.0721514jes.

26 M. Naylor Marlow, J. Chen and B. Wu, Degradation in parallel-connected lithium-ion battery packs under thermal gradients, Commun. Eng., 2024, 3, 1, 2, DOI: 10.1038/s44172-023-00153-5.

27 M.-S. Wu, C.-Y. Lin, Y.-Y. Wang, C.-C. Wan and C. R. Yang, Numerical simulation for the discharge behaviors of batteries in series and/or parallel-connected battery pack, Electrochim. Acta, 2006, 52, 3, 1349–1357, DOI: 10.1016/j.electacta.2006.07.036.

28 J. Brand, M. H. Hofmann, M. Steinhardt, S. F. Schuster and A. Jossen, Current distribution within parallel-connected battery cells, J. Power Sources, 2016, 334, 202–212.

29 T. Bruen and J. Marco, Modelling and experimental evaluation of parallel connected lithium-ion cells for an electric vehicle battery system, J. Power Sources, 2016, 310, 91–101.

30 X. Liu, W. Ai, B. Wu and W. Ai, The effect of cell-to-cell variations and thermal gradients on the performance and degradation of lithium-ion battery packs, Appl. Energy, 2019, 251, 113381, DOI: 10.1016/j.apenergy.2019.04.108.

31 E. Hosseinzadeh, S. Arias, M. Krishna, D. Worwood, A. Barai, D. Widanalage and J. Marco, Quantifying cell-to-cell variations of a parallel battery module for different pack configurations, Appl. Energy, 2021, 282, 115859.

32 W. Shi, X. Hu, C. Jin, J. Jiang, Y. Zhang and T. Yip, Effects of imbalanced currents on large-format $LiFePO_4$/graphite batteries systems connected in parallel, J. Power Sources, 2016, 313, 198–204.

33 M. Fleckenstein, O. Bohlen, M. A. Roscher and B. Bäker, Current density and state of charge inhomogeneities in Li-ion battery cells with $LiFePO_4$ as cathode material due to temperature gradients, J. Power Sources, 2011, 196, 10, 4769–4778.

34 National Highway Traffic Safety Administration, Tesla recalls 53,000 Model S vehicles due to battery module failure risk, U.S. Department of Transportation, 15 April 2023, https://www.nhtsa.gov/recalls/tesla-model-s, [Accessed 1 October 2024].

35 M. Woody, M. Arbabzadeh, G. M. Lewis, G. A. Keolein and A. G. Stefanopoulou, Strategies to limit degradation and maximize Li-ion battery service lifetime – critical review and guidance for stakeholders, J. Energy Storage, 2020, 28, 101231.

36 R. Hausbrand, G. Cherkashinin, H. Ehrenberg, M. Gröting, K. Albe, C. Hess and W. Jaegermann, Fundamental degradation mechanisms of layered oxide Li-ion battery cathode materials: methodology, insights and novel approaches, Mater. Sci. Eng., B, 2014, 192, 3–25, DOI: 10.1016/j.mseb.2014.11.014.

37 C.-F. Chen, P. Barai and P. P. Mukherjee, An overview of degradation phenomena modeling in lithium-ion battery electrodes, Curr. Opin. Chem. Eng., 2016, 13, 82–90, DOI: 10.1016/j.coche.2016.08.008.

38 M. Börner, F. Horsthemke, F. Kollmer, S. Haseloff, A. Friesen, P. Niehoff, S. Nowak, M. Winter and F. M. Schappacher, Degradation effects on the surface of commercial $LiNi_{0.5}Co_{0.2}Mn_{0.3}O_2$ electrodes, J. Power Sources, 2016, 335, 45–55, DOI: 10.1016/j.jpowsour.2016.09.074.

39 M. M. Kabir and D. E. Demirocak, Degradation mechanisms in Li-ion batteries: a state-of-the-art review, Int. J. Energy Res., 2017, 41, 15, 1963–1986, DOI: 10.1002/er.3762.

40 M. R. Palacín, Understanding ageing in Li-ion batteries: a chemical issue, Chem. Soc. Rev., 2018, 47, 4924, DOI: 10.1039/c7cs00889a.

41 M. Jiang, D. L. Danilov, R.-A. Eichel and P. H. L. Notten, A review of degradation mechanisms and recent achievements for Ni-rich cathode-based Li-ion batteries, Adv. Energy Mater., 2018, 8, 17, 1800233, DOI: 10.1002/aenm.201800233.

42 J. Miao, Review on electrode degradation at fast charging of Li-ion and Li metal batteries from a kinetic perspective, Electrochem., 2023, 3, 1, 156–180, DOI: 10.3390/electrochem3010013.

43 N. Nitta, F. Wu, J. T. Lee and G. Yushin, Li-ion battery materials: present and future, Mater. Today, 2015, 18, 5, 252–264, DOI: 10.1016/j.mattod.2014.10.040.

44 G. Vennam, A. Sahoo and S. Ahmed, A survey on lithium-ion battery internal and external degradation modeling and state of health estimation, J. Energy Storage, 2022, 52, 104720, DOI: 10.1016/j.est.2022.104720.

45 H. Rauf, M. Khalid and N. Arshad, Machine learning in state of health and remaining useful life estimation: theoretical and technological development in battery degradation modelling, Renew. Sustain. Energy Rev., 2022, 156, 111903, DOI: 10.1016/j.rser.2021.111903.

46 J. Li, B. Liu, S. Li, D. Hu, L. Wang and J. Xu, Mechanistic modeling of Li plating in lithium-ion batteries, J. Power Sources, 2022, 521, 230936, DOI: 10.1016/j.jpowsour.2022.230936.

47 X.-G. Yang, Y. Leng, G. Zhang, S. Ge and C.-Y. Wang, Modeling of lithium plating induced aging of lithium-ion batteries: transition from linear to nonlinear aging, J. Power Sources, 2017, 360, 28–40, DOI: 10.1016/j.jpowsour.2017.05.110.

48 M. T. Lawder, P. W. C. Northrop and V. R. Subramanian, Model-based SEI layer growth and capacity fade analysis for EV and PHEV batteries and drive cycles, J. Electrochem. Soc., 2014, 161, 14, A2099–A2108, DOI: 10.1149/2.1161412jes.

49 A. Weng, E. Olide, I. Kovalchuk, J. B. Siegel and A. Stefanopoulou, Modeling battery formation: boosted SEI growth, multi-species reactions, and irreversible expansion, J. Electrochem. Soc., 2023, 170, 9, 090523, DOI: 10.1149/1945-7111/aceffe.

50 M. Safari, M. Morcrette, A. Teyssot and C. Delacourt, J. Electrochem. Soc., 2009, 156, A145–A153, DOI: 10.1149/1.3043429.

The codes will be made available on GitHub at kshah-ua/SPM-SEI-sim-code---multi-cell-system, and all the data, including raw data, will be shared via Open Science Framework at https://osf.io/92szb/?view_only=c2743d5ea5c1423dae292dcafeffbe53.

Energy Advances Accepted Manuscript